RADIOFREQUENCY COIL DESIGN AND APPLICATION TO MAGNETIC RESONANCE IMAGING AND CONTROL OF MICRO-BEADS

by

William Marshall Potter

(Under the Direction of Qun Zhao)

ABSTRACT

Radio Frequency coil development, one component of a functioning magnetic resonance imaging (MRI) system, has evolved since the beginning of MRI into a very diverse area. Today for example, transmit and receive coils, volume and surface coils, and single channel and multiple channel coils are all included. Coils are created to fit the particular needs of specific research purposes, taking into consideration advantages and disadvantages of different types of coils. The shape and size of the anatomy to be scanned and the nuclei from which signal will be acquired are a few of the various considerations to account for. The majority of this work details the development of a new dual-tuned birdcage coil and its evaluation, by comparing it to a commercial dual-tuned surface coil. Simulations of the new design are presented, as compared to an existing dual-tuned coil, along with experimental results from the completed coil. A secondary focus of this work details the construction of a three axis electromagnetic coil designed to drive magnetic micro-beads through a fluid. The creation of a rotating magnetic field that would turn helical structures is discussed followed by simulations on creating a rotating magnetic field in any direction with coils aligned in the three Cartesian directions.

INDEX WORDS: Magnetic Resonance Imaging and Spectroscopy, Chemical Shift Imaging, Radio Frequency Coil Design, Birdcage Coil, Dual-Tuned, Micro-Beads

RADIOFREQUENCY COIL DESIGN AND APPLICATION TO MAGNETIC RESONANCE IMAGING AND CONTROL OF MICRO-BEADS

by

William Marshall Potter

B.S., The University of Georgia, 2005

A Dissertation Submitted to the Graduate Faculty of The University of Georgia in Partial Fulfillment of the Requirements for the Degree

DOCTOR OF PHILOSOPHY

ATHENS, GEORGIA

2012

RADIOFREQUENCY COIL DESIGN AND APPLICATION TO MAGNETIC RESONANCE IMAGING AND CONTROL OF MICRO-BEADS

by

William Marshall Potter

Major Professor:	Qun Zhao
Committee:	Uwe Happek Kevin McCully Leidong Mao Heinz-Bernd Schuttler

Electronic Version Approved:

Maureen Grasso
Dean of the Graduate School
The University of Georgia
August 2012

ACKNOWLEDGEMENTS

I would like to thank my fellow graduate students, Dr. Jason Langley, Mr. Terence Ryan, Mr. Joonsang Lee, Mr. Luning Wang, and Mr. Tomas Koci for both their help and encouragement, Mrs. Kim Mason for everything she taught me about MRI, and my advisor, Dr. Qun Zhao for his guidance and his words of wisdom throughout my study. I would also like to acknowledge support from NIH Child Health and Human Development Research Grant HD039676 and Dr. Kevin McCully.

TABLE OF CONTENTS

LIST OF FIGURES

LIST OF TABLES

CHAPTER 1

INTRODUCTION TO THE PHYSICS OF MAGNETIC RESONANCE

Magnetic Resonance Imaging (MRI) brings together many principles and techniques to generate the images that we are all familiar with today. In this chapter I will briefly review the development of MRI and discuss the concepts and coils that enable MRI systems to function. Focus will be put on the RF transmit/receive component of the MRI system which includes the generation of the B_0 field, gradient fields, and RF fields.

1.1 Background of Magnetic Resonance Imaging

It was in 1976 that the first MRI image was acquired from a human by Sir Peter Mansfield in England. This first MRI was only a very small cross-section of a human finger, but it was the culmination of techniques developed over the past half century [1, 2]. The principles of his experiment go back to varying gradient fields, nuclear magnetic resonance (NMR), and even the discovery of the spin characteristics of nuclei.

Mansfield, along with Paul Lauterbur won the Nobel Prize for their contributions to the field of magnetic resonance in 2003. They played a pivotal role in the development of the mathematical analysis for image reconstruction and forming images from an experiment by adjusting gradient fields for spatial encoding, respectively [1, 3]. Lauterbur used the fact that the rate at which the spin of a nucleus precesses depends on the strength of the uniform magnetic field, B_0, and so by introducing a gradient to the field, he could control the region from which

signal was collected [3-6]. This made it possible to localize a signal to a specific region and therefore spatially encode the acquired signal. Lauterbur's technique of zeugmatography, which is the combining of a magnetic field and gradients to produce a two-dimensional image, was later replaced by a faster acquisition method introduced by Mansfield where in one acquisition, an entire slice was excited followed by rapidly changing gradient fields to create spatial encoding.

The groundwork for these developments in magnetic resonance goes back to the 1940s when Felix Bloch and Edward Purcell described the relaxation of perturbed atomic nuclei in a magnetic field after which the study of the chemical structure of molecules was made possible. A notable finding of their experiments was that the magnetization vector did not depend on the nucleus' movement. Their experiments were the first NMR experiments and were executed with very different methods. Bloch's experiment was more like modern NMR experiments using a water sample and a constant B_0 field while the alternating, radiofrequency (RF) field was varied until resonance was reached [4]. Purcell, in a coincident effort, used a paraffin sample, a varying B_0 field, and a constant RF field [5]. Though they both studied the relaxation of nuclei in a magnetic field it was Bloch who is credited with what is known as the Bloch equation that describes the relaxation of a particular nucleus as it precesses in a magnetic field. Both men were awarded the 1952 Nobel Prize for their development of magnetic precision measurement.

It could be argued that the whole of the development of MRI rests on the shoulders of Isidor Rabi who used the work of Otto Stern and Walther Gerlach to conduct experiments to measure the resonant frequency of hydrogen nuclei by observing its interaction with a magnetic field. This is the most fundamental idea around which modern MRI is based. For a nucleus to be compatible with magnetic resonance experiments, it must have an odd number of protons and neutrons so that its total nuclear spin is a factor of one-half. In the absence of a magnetic field, a

spin ½ nucleus' magnetization will have a random distribution in space. However, in a magnetic field, the parallel state is at a slightly lower energy level and therefore slightly more spins align parallel as opposed to antiparallel. This gives a net magnetization in the macroscopic scale.

Combining all of the factors that lead to modern MRI, we have MRI sensitive nuclei within a strong constant magnetic B_0 field. An RF magnetic field, orthogonal to B_0, is applied to the nuclei to knock its magnetization out of alignment by some angle. With the help of gradient fields the signal can be spatially encoded and acquisition can be done one slice at a time. And finally, after mathematically reconstructing the data, an image is formed that contrasts tissues or materials with either varying concentrations of the target nucleus or varying relaxation times dependent on the tissue or material.

1.2 Generation of Magnetic Fields

The modern MRI system has three major components that are the concern of this work, the static magnetic field, B_0; the transmit/receive RF system, B_1; and the gradient fields. As was previously alluded to, the B_0 field is responsible for aligning the spins of the nuclei to be studied. This produces a net magnetization that is parallel to the B_0 field. Next, the RF transmit/receive system excites the nuclei and gathers the signal from the precessing spins. The last major system introduces gradients in the magnetic field so that spatial encoding is possible. These systems use three very different types of coils to produce each desired effect. It would be worthwhile to start from the beginning to describe how magnetic fields are produced.

Hans Christian Oersted, in 1820, discovered a relationship between electricity and magnetism. By using a compass needle as an indicator of magnetic field, he found that the compass deflects when placed next to a wire carrying a current such that the needle points

tangent to a circle centered on the wire. The deflection can also be described by the right-hand-rule. By assigning the right hand thumb to be the current in the wire, the fingers wrap around the wire, when closed, in the direction of the magnetic field that is produced. The magnitude of the field at a distance *r* from the wire is given by

$$B = \frac{\mu_0 I}{2\pi r} \tag{1.1}$$

where *B* is the magnetic field generated, μ_0 is the permeability of free space, and *I* is the current in the wire. This is the most basic principle used to make every coil used in MRI. The only difference between each system is the geometry or configuration used. With any geometry, the net magnetic field at a point is the sum of the magnetic fields from all sources at that point. Next, let's consider a solenoid. A solenoid is a wire coiled into the shape of a cylinder. This type of design can produce a relatively uniform magnetic field within the solenoid. The field inside of the solenoid at the center on the axis is

$$B = \mu_0 nI \tag{1.2}$$

where *n* is the number of turns per unit length. The B_0 field could be generated essentially by a very large superconducting solenoid in typical closed imaging systems, however this isn't a good practical solution because for a solenoid to give a uniform magnetic field, its length should be large compared to its diameter. Therefore, the modern approach to creating the B_0 field uses a different design (arranged in patterns as seen in figure 1 and to be discussed next) to make the magnetic field inside of the coil as homogeneous as possible. Sometimes correcting fields, or shimming fields, are also needed to correct for small variations in this B_0 field.

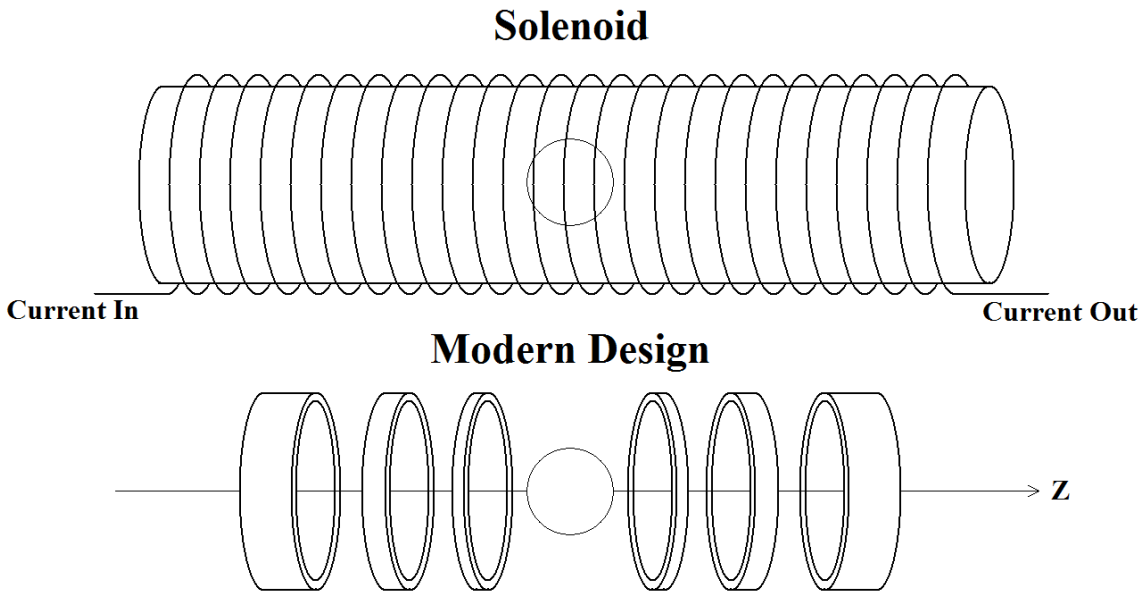

Figure 1.1: Unlike the solenoid design (top), which needs to have a length much greater than the radius to produce a homogeneous field in the center, the modern design (bottom) uses a series of smaller multi-layer solenoid coils to produce a homogeneous field in the center.

There are a few configurations of coils that are designed with loops of current carrying wire separated by some distance that are used to produce the strong B_0 field and gradient fields. To start, the equation for the magnetic field produced by a single loop of current carrying wire along the centered axial line is

$$B_z = \frac{\mu_0 I a^2}{2(a^2+z^2)^{3/2}} \tag{1.3}$$

where a is the radius of the loop centered at zero, I is the current in the loop and μ_0 is the permeability of free space. The Helmholtz pair uses two loops of wire carrying current in the

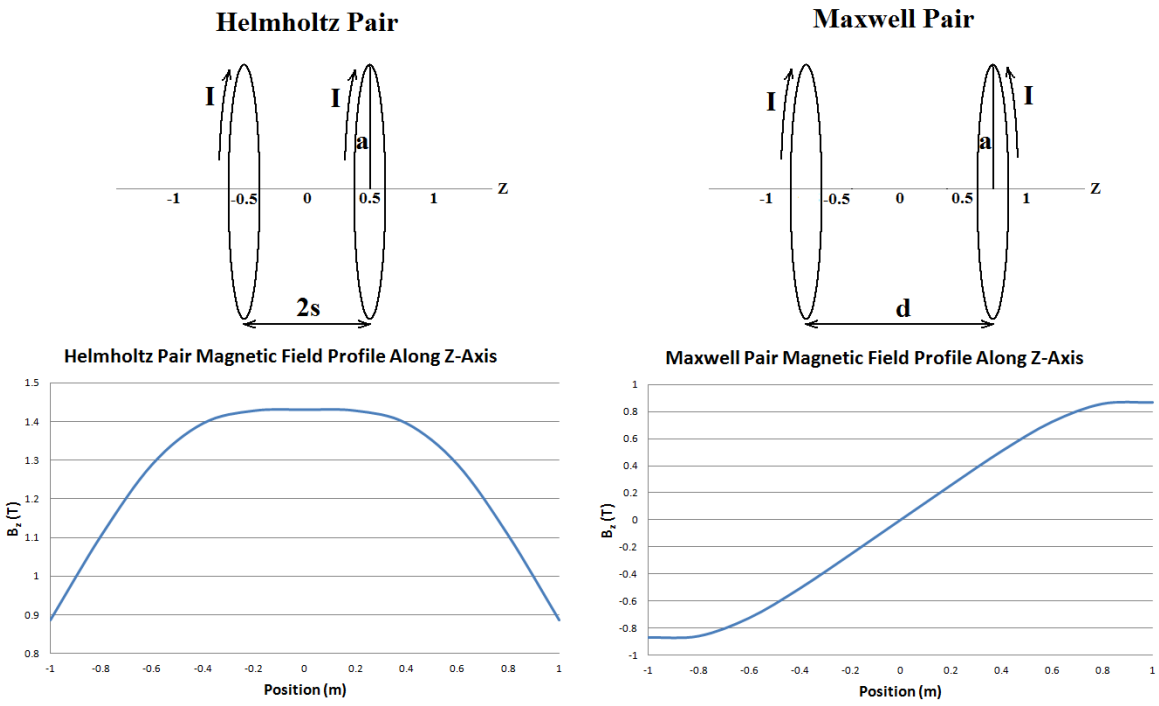

Figure 1.2: A Helmholtz Pair on the Left with the ideal spacing, when a=2s, for a maximized homogeneity between the coils. A Maxwell Pair, as seen on the Right, has an optimum gradient with the spacing between the two coils, d, equal to $\sqrt{3}$a. Each magnetic field profile is the one along the z-axis and the current flowing through each loop was chosen for simplicity such that $\frac{\mu_0 I}{2} = 1$.

same direction. This type of setup is used in producing homogeneous B_0 fields, as seen in the magnetic field profile in figure 1.2. It is governed by the equation

$$B_z = \frac{\mu_0 I a^2}{2(a^2+(z+s)^2)^{3/2}} + \frac{\mu_0 I a^2}{2(a^2+(z-s)^2)^{3/2}} \tag{1.4}$$

where the coils are located at $\pm s$. The homogeneity from this coil is maximized when the separation of each loop is equal to the radius of the loops, or $a = 2s$. A common method of creating a homogeneous region in the center is to use a few of these Helmholtz pairs of varying

strength and varying distances so that the net homogeneity is greater than that created from a single pair.

The second type of configuration is the Maxwell pair, seen in figure 1.2. This pair uses two loops of current carrying wire separated by some distance except this time the current in each loop flows in opposite directions from each other. This produces a magnetic field gradient along the axis of the two coils governed by the equation

$$B_z = \frac{-\mu_0 I a^2}{2(a^2+(z+s)^2)^{3/2}} + \frac{\mu_0 I a^2}{2(a^2+(z-s)^2)^{3/2}} \quad (1.5)$$

where this time, the ratio of the coil radius to the coil spacing is 1 to $\sqrt{3}/2$ for the most uniform gradient field as seen in figure 1.2. A uniform gradient field for this coil pair has a constant, non-zero first derivative of the magnetic field along the z-axis. The optimum distance is where the lowest order perturbation to the linear gradient is zero. The third pair of coils, the Golay pair, which is seen in figure 2, produces gradients in the x- and y-directions. They have shapes that can be described like saddles and the position that gives the most uniform gradient field in the x- and y- directions for these coils is shown in figure 1.3.

1.3 The RLC Circuit

The third major component of the modern MRI system is the transmit/receive RF coil. Unlike the previously described direct current or static magnetic field coils, the RF coil must create a rotating magnetic field at the proper resonant frequency of the nucleus to be studied. This is not a simple task.

To understand the RF coil, a brief description of its components and basic mechanisms is needed. The components of any RF coil include a capacitance (C), inductance (L), and inevitably some resistance (R) forming an RLC. Consider a circuit under ideal conditions where the

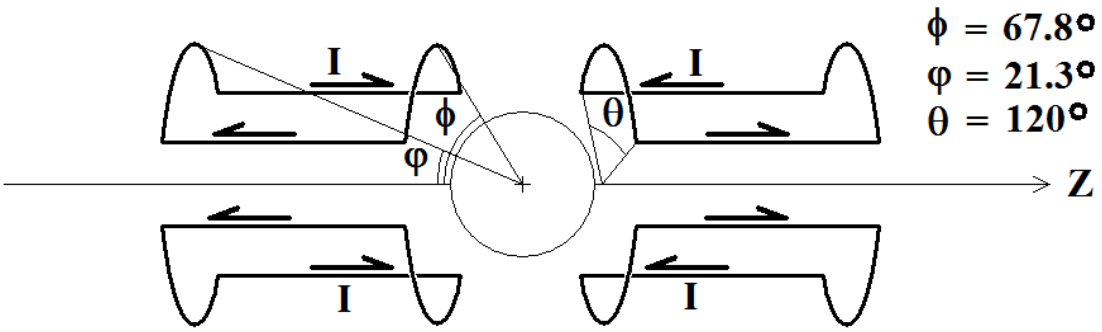

Figure 1.3: The Golay Pair uses the symmetry of the system to cancel out the magnetic fields produced along the z-direction leaving only the gradient fields produced in the x- and y-directions. Inside the circular region of interest (ROI), this particular coil orientation produces a uniform gradient in the transverse plane to the z-axis from top to bottom.

resistance through the conductor and inductor is zero. What remain are capacitance and inductance. After charging the capacitor and then closing the circuit, the charge on the capacitor will flow through the circuit through the inductor with some changing current. The potential difference across the capacitor must equal the potential difference across the inductor.

$$V = \frac{Q}{C} = -L\frac{\partial I}{\partial t} \tag{1.6}$$

where V is the potential difference, Q is the charge on the capacitor at some instant, and I is the current through the inductor at the same instant. When the capacitor is completely discharged, the current through the inductor will be at a maximum, but its change over time will be zero. A maximum current through the inductor also means a maximum magnetic field generated by the inductor. The flowing charge continues through the circuit and once again fully charges the capacitor. In an ideal case, this oscillation, called an LC oscillation, continues unhindered. The frequency of oscillation is given by equation 1.7.

$$f = \frac{1}{2\pi\sqrt{LC}} \tag{1.7}$$

Adding resistance to the closed circuit merely adds a damping factor to the equation. The next step is to consider an RLC circuit driven by an alternating current at resonance. The root mean square (rms) current in the circuit is given by

$$I_{rms} = \frac{V_{rms}}{\sqrt{R^2+(\omega L-\frac{1}{\omega C})^2}} \tag{1.8}$$

where V_{rms} is the root mean square of the alternating potential difference across the source. This equation is an adaptation of Ohm's Law, $V = IR$, which relates the current, potential, and impedance (including both resistance and reactance) in a circuit. RF coils use this type of circuit where they are driven by some alternating source. The current through the circuit reaches a maximum when

$$\omega L - \frac{1}{\omega C} = 0 \tag{1.9}$$

solve for ω to get

$$\omega_0 = \frac{1}{\sqrt{LC}} \tag{1.10}$$

where ω_0 is the driving voltage angular frequency when the circuit is in resonance. The resonant frequency is then

$$f_0 = \frac{\omega_0}{2\pi} \tag{1.11}$$

This concludes the discussion of the components of the RF coil. The oscillation of electromagnetic field energy between the capacitance and the inductance in the circuit creates the alternating current which ultimately produces the oscillating magnetic field required to excite the spins of the nuclei.

1.4 Radiofrequency Coils

The earliest RF coils were what we now call surface coils. They consisted of a single loop of conductor (large gauge wire) and capacitance symmetrically placed around the loop. These coils were used in pairs and situated orthogonally to each other so that the transmit coil didn't interfere with the receive coil.

The surface coil in modern MRI has been modified to form what is called a phased array coil, where multiple surface coils are connected to individual power input channels from the MRI system. This type of multi-channel coil surrounds the sample with surface coils each connected to a different channel and generates a high signal to noise ratio at places close to each of the surface coils. Simultaneous data acquisition through multiple channels allows for quicker scan times, but reconstruction is complicated.

The birdcage coil was developed in an effort to create a coil with improved homogeneity over previously used saddle coils. The basic birdcage design consists of axially directed rungs or legs that are connected on each end by rings called endrings. The initial steps towards its creation solidified its cylindrical shape, its symmetry about the z-axis, and its rung and endring design. Incidentally, these characteristics pointed the developers toward quadrature excitation as opposed to linear excitation. The first birdcage coil that was used was a low-pass (LP) coil which means that capacitors were located at the midpoint of the legs of the coil. When this type of coil is driven by a single excitation (e.g. a sinusoidal) source at one (linearly polarized), or two sources separated by a phase shift of 90 degrees (circularly polarized or quadrature), where a source is usually placed across a capacitor, the power oscillates between the capacitance and the intrinsic inductance of the coil (a conductor) producing a sinusoidal current distribution around the legs of the coil. This sinusoidal current is what produces either a linearly or circularly

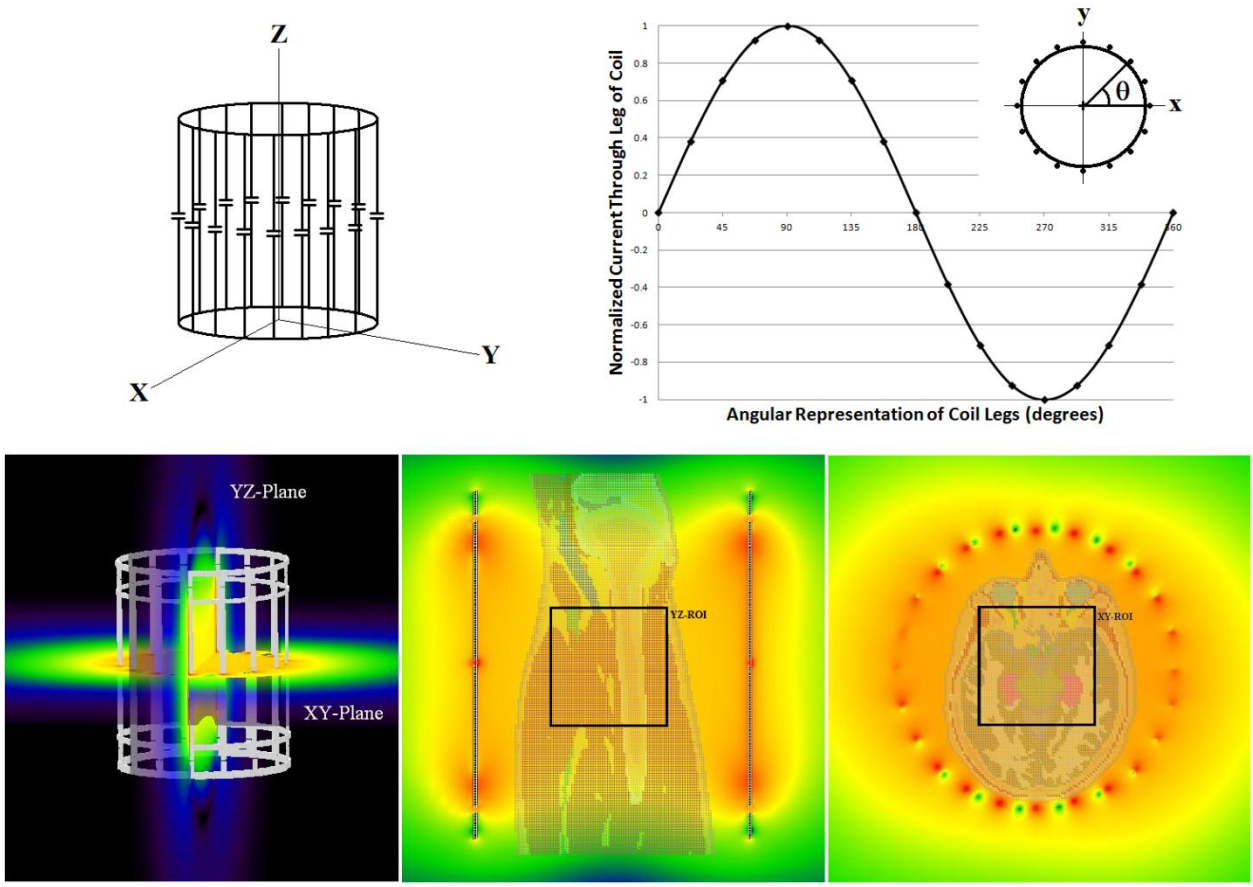

Figure 1.4: Top: Displayed are a 16-leg low-pass (LP) birdcage coil (single-tuned, 2-ring) and current distribution that is produced on resonance around each leg of the coil. Bottom: A 4-ring dual-tuned birdcage coil and two configurations from simulation trials depicting magnetic field projections onto the yz- and xy-planes (on a simulated human thigh, Middle, and human head, Right).

polarized B_1 field in the transverse plane. Two variations of this type of coil include the high-pass (HP) coil and the band-pass coil. The overall structure of these two variations is the same, with the exception of the placement of the capacitors. The HP coil has capacitors located on the endrings and the band-pass coil has capacitors located on both the legs and endrings. This variation of capacitor placement has an effect on the resonant modes of the coils, however the

current distribution for the primary mode remains sinusoidal. Figure 1.4 depicts the current distribution for the primary mode of a LP birdcage coil along with the RF field orientation and distribution in a simulation for a 4-ring dual-tuned birdcage coil.

The next step in the evolution of coils is to acquire localized multinuclear spectroscopic information from nuclei other than Hydrogen (^{1}H). A dual-tuned coil can accomplish this. The coil acquires an image from the ^{1}H signal followed by an acquisition of spectral signal from another nucleus (e.g. ^{31}P) from the same region. Unlike ^{1}H, other nuclei have both much lower concentrations in the human body and smaller gyromagnetic ratios than ^{1}H. To get a better SNR, the spectral signal needs to either come from a larger region (more spins) or more scans need to be averaged. Also, it is necessary to have a coil acquire a ^{1}H signal to localize the spectral data to an image or to adjust the homogeneity of the non-hydrogen signal. There are many studies that involve non-Hydrogen acquisition and not having to switch coils or patient positions during a scan is desirable. Apart from other multinuclear experiments with Carbon-13, Fluorine-19, and Sodium-23, just to name a few, Phosphorus-31 is a very common element for multinuclear experiments looking at biochemical indicators of various processes within the human body [7-25]. Some various types of dual-tuned birdcage coils include the 4-ring birdcage coil, the concentric birdcage coil, and the alternating rung birdcage coil.

The 4-ring birdcage design maximizes the sampling volume of the inner multinuclear coil. However, the sampling volume from the outer ^{1}H coils is less than ideal because signal is acquired typically from the center of the entire coil. When acquiring ^{31}P signal for example, the inner coil is centered on the target region. Though the outer coils are directly connected, they play no role in ^{31}P measurements. The two outer ^{1}H coils are, as a consequence of the positioning, far from the target area that is at the midpoint of a line connecting the two outer

coils. Refer to figure 2.1. As indicated in ref [25], the 4-ring design utilizes the coupling between the outer coils through the inner coil, for ^{1}H acquisition, by way of producing a corotating and counterrotating mode in the outer coils. Only the corotating mode produces a current flow through the inner coil and therefore a rotating B_1 magnetic field at the resonant frequency of ^{1}H at the center of the coil.

Concentric birdcages maximize the sampling volume for each nucleus's coil [26, 27]. However, when the coils share the same sampling volume the inductive coupling is very strong between the two coils which might obscure the primary mode. The close proximity of the capacitors to each other can also create interference to the B_1 homogeneity by way of producing electric field inhomogenities. By building one coil as a LP coil (placing capacitors at the midpoint of each leg) and the other as a HP coil (placing capacitors between legs on the endring), the capacitors can be spaced apart from each other. Offsetting one coil by half the angle between two legs can also minimize the coupling between the coils [27].

An alternating rung design gives a maximized and identical sampling volume, but effectively reduces the number of birdcage legs by half and as a result, decreases field homogeneity [28, 29]. A trap is placed on every other leg in order to block the resonant frequency of one nucleus while allowing that of the other to pass. Dual-tuning is achieved with the idea that the impedance of the legs with the traps is high as seen by the current that flows around the coil, which is from the same frequency as that of the traps. This allows for half the legs to operate at one frequency (corresponding to one nucleus) and the other half to operate at another frequency (corresponding to the other nucleus). The resonant frequencies need to be far apart so that the trap can have large impedance for one resonant frequency but not the other.

Without the trap in this design, out of phase currents from the higher resonant frequency can flow along the legs tuned for the lower frequency.

The primary difficulty towards the creation of these kinds of dual-tuned birdcage coils is that the process of making the coil compatible with the MRI scanner (which drives the coil and acquires data from the sample) is very tedious. Particularly, the tuning and matching of such a dual-tuned coil is a very time consuming iterative process adjusting the frequency of one coil and then the other. Iterations are required because altering one coil affects the other. If there was a single coil that could solve every research need, then it would not matter how tedious the device was to build. The process could be done very carefully once and then duplicated in an assembly line fashion. However, due to the diversity of uses and particular needs of each situation, each coil would have to be a custom build. Therefore, an iterative process for tuning and matching (that requires many rounds of adjusting capacitances for each coil), that adds to an already complex birdcage coil design, increases the chances of human errors and flaws that would lead to unwanted interference or coupling within the coil itself and ultimately poor signal acquisition quality.

1.5 Overview of the Dissertation

The focus of this work as a whole is directed towards the development and evaluation of radiofrequency/electromagnetic coils for use in MRI. The simulations of, and methods for, constructing a new dual-tuned birdcage coil are detailed in the following chapters as well as the creation of an electromagnetic coil to drive micro-beads.

The new dual-tuned birdcage coil, called the split birdcage coil, is modeled after an existing dual-tuned birdcage coil that is designed to measure signal from Phosphorus as well as

Hydrogen. It is designed in such a way as to optimize the collection of signal from the ^{31}P nuclei. Chapter 2 deals with the split birdcage coil, including both the simulations and the experimental evaluation of the coil in the MRI scanner. The techniques for evaluation include comparison to a pre-existing dual-tuned birdcage coil in the simulations and an experimental comparison to a commercially available dual-tuned surface coil.

In Chapter 3, the working split birdcage coil is further used for a baseline study to acquire data from ten human subjects. The efficacy of the coil's acquisition of ^{31}P is tested in conjunction with a muscle/fat segmentation method for the anatomical (^{1}H) images.

The construction of a new RF coil provides insights that are used in Chapter 4 to describe the creation of an electromagnetic coil that is used in a very constricted environment to control micro-beads. The three-axis Helmholtz coil interfaces with a computer which controls the current sent to each part of the coil in order to produce an aligning field and a rotating field in the center of the coil.

Lastly, Chapter 5 relates the conclusions made from this work and future aims and goals for the use of these coils.

CHAPTER 2

THE SPLIT BIRDCAGE COIL

In this chapter, I introduce and evaluate a new dual-tuned ($^{1}H/^{31}P$) birdcage coil, referred to as split birdcage coil. Both simulations and MR experiments on a phantom and human skeletal muscles were used to demonstrate its operation. This design simplifies the practical matters of tuning and matching which makes the coil easy to reproduce. First, simulations were run with the Finite Difference in Time Domain (FDTD) method to compare the magnetic field strength and homogeneity of the design's hydrogen (^{1}H) coils with that of a previously published 4-ring birdcage coil. Following simulations, MR experiments were conducted to compare the new design with a currently available commercial dual-tuned surface coil for signal to noise ratio (SNR) as well as homogeneity for the phosphorous (^{31}P) coil.

2.1 Introduction of the Problem and Background

Dual-tuned ($^{1}H/^{31}P$) birdcage coils are a well known and widely used tool for magnetic resonance spectroscopy (MRS) [11, 12, 21, 22, 24-34]. They provide a uniform RF magnetic field inside the coil and can be made to fit most anatomies [21, 35-42]. The classification for and development of dual-tuned coils has been explored with various nuclei [27], at different field strengths [29], and by acquiring spectra from animals [33] to the human brain [11, 21, 24, 25]. A two-in-one structure of such a coil solves practical issues that arise from having to use two separate coils or having to reposition the subject in the scanner. When spectral signal is localized

to a specific region of tissue, it becomes very important to acquire a suitable anatomical image along with a multinuclear spectrum from the exact same tissue.

MRS can be used for the study of an assortment of different metabolites in the human body. Oxidative metabolism indices, such as kinetic changes in phosphocreatine (PCr), are important indicators of biochemical processes [14, 16]. MRS of phosphorous (^{31}P MRS) is well suited to monitor these processes in both skeletal muscles and neuronal synaptic development in human brains [7-10, 15, 17, 19, 20]. However, the ^{31}P MRS signal sensitivity is usually low due to low concentrations of the nucleus, a relatively small gyromagnetic ratio compared to ^{1}H, and magnetic field inhomogeneity from currently available commercial surface coils. Birdcage coils, on the other hand, give homogeneous magnetic fields and high efficiency at low specific absorption rates (SARs) [35-43]. This point has been demonstrated in the past by simulating B_1 magnetic field maps in order to analyze homogeneity [37, 38, 40, 42] along with SAR calculations with a simulated model of the human body loaded in the coil [36, 39, 41].

The practicality of building a dual-tuned birdcage coil is not trivial and can be a complex endeavor to approach due to many factors. For example, what type of birdcage is the easiest to tune and match, which kind gives the best homogeneity, the largest sampling volume, and a max or min coupling. "Coupling" is used loosely here in that coupling from two coils, directly connected, should be minimized to reduce the procedure of iterative tuning. The other sense of the word coupling refers to two coils (^{1}H coils for example) that couple through a central coil (^{31}P) to increase the signal sensitivity of the first two coils. This type of coupling should be maximized in order to acquire the best signal. The structure of the coil (e.g., number of legs/rings, dimensions, ratio of length to diameter) is crucial to effective signal acquisition from two different nuclei. Existing examples of dual-tuned birdcage coils include the 4-ring birdcage

[21, 25], concentric birdcages [26, 27], and the alternating rung birdcage [28, 29]. All of these either share endrings or share enclosed sampling volumes.

In this study of human skeletal muscle metabolism, the 4-ring design was initially chosen for its large multinuclear sampling volume. However, it was found that construction of this coil required an iterative process of tuning the inner and outer coils, until the desired resonant frequency for each was reached, and this makes the coil hard to reproduce. This coil is an effective dual-tuned coil because the impedance from the capacitors of the outer coils are large as seen by circulating power at the resonant frequency of the inner coil. Therefore power from excitation of the inner coil will stay in the inner coil [25]. The 4-ring design is unique because its outer coils use the connection of the inner coil to produce a corotating and counterrotating current distribution, reflected as a frequency split in the primary resonance mode.

To overcome the tuning difficulty and make the coil easily reproducible, the creation of a split birdcage coil was proposed. The purpose of the split design is to still use the coupling through the center or inner coil, but to separate the coils' direct connection to allow for the individual tuning of each coil.

Another goal of this study was to verify some well known concepts concerning birdcage coils by introducing the split birdcage coil design and by comparing it against a commercially available dual-tuned surface coil. The intention was to find out whether the new design of birdcage coil could compete with the commercial coil that is used for most multinuclear spectroscopy needs. Surface coils have been used to measure PCr signal in the vastus lateralis muscle in the thigh. This muscle typically has the thinnest section of fat covering it so that it is the closest muscle in the thigh to the coil [17]. In order to acquire data from another muscle or muscle group, the coil must be shifted and repositioned [9].

In this work, a comparison for the coils' sensitivity or magnetic field homogeneity and SNR is presented as simulation between the 4 ring birdcage and the split birdcage as experiment between the split birdcage coil and a commercial flex surface coil for their ability to localize and characterize a single muscle. All anatomical and spectroscopic signals were acquired from a phantom and a human volunteer using a GE 3T HDx magnet.

2.2 Innovation for the New Coil and Theory

In principle, the split birdcage design utilizes inductive coupling between the outer coils and the inner coil in order to produce the same effect of corotating and counterrotating modes as the 4-ring coil design. The coupling occurs between every mesh loop from one coil to every mesh loop in the adjacent coil. However, the strongest coupling occurs in the z-direction between endrings and is related to the flux from one endring to the next as described by Lenz's Law. The sinusoidal current that is produced on the legs of the birdcage, also travels around the endrings for the coil that is being excited. Lenz's Law says that magnetic flux through a closed loop will produce a current in a neighboring loop that will try to oppose the changing magnetic field. This induced current in the endring produces a current along the legs of the inner coil and thus a rotating magnetic field that is greater and more homogeneous than a rotating magnetic field produced by two ^{1}H coils with no ^{31}P coil between them.

The split birdcage coil was constructed with a large acrylic tube for the frame of the coil. Heat resistant tape and copper tape were laid down in the pattern of three separated 8-leg birdcages on a plastic film and wrapped around the acrylic tube. In this work a split design coil was built for its large multinuclear sampling volume, its use of inductive coupling between the coils, and its full use of all of the legs in the coil. However, in contrast to the simulations of a LP-

LP coil, a LP-HP design was chosen because the value of the capacitors used in the HP outer coils is larger than the equivalent LP birdcage with the same dimensions. Also, it is easier to obtain symmetry around the HP coil, because there are twice as many capacitors to work with. The prototype was built as an adaptation of this coil with an initial space of 0.4cm between the inner coil and the HP outer coils. Additional components to our design include two quadrature couplers, multi-component matching circuits and phase shifters, non-magnetic coaxial cable, and a protective plastic shell.

The inner ^{31}P coil was tuned to 51.7MHz with a capacitance at each leg of 21.2pF. The inner coil was excited with quadrature excitation. Two equal length coaxial cables were used to deliver power to the coil at two capacitors that were 90 degrees from each other, yielding an improvement in SNR of the square root of 2 over linear excitation. A quadrature coupler (30MHz to 88MHz, Innovative Power Products, Holbrook, NY, USA) was used for this purpose. A T-shaped phase shifter was used for the inner ^{31}P coil to correct the phase shift to exactly 90 degrees. The two outer ^{1}H coils were each tuned to 127.75MHz. Finally, two matching circuits were used to match each coil to 50Ohms. Excitation on the ^{1}H coils gave unloaded and loaded Q-factors of 125 and 90 respectively, while excitation on the ^{31}P coil gave unloaded and loaded Q-factors of 89 and 25 respectively.

A large bottle 18cm in diameter and 25cm in length filled with a 100mM concentration of KH_2PO_4 was used for tuning. Tuning was also done with the human leg as a loading to ensure a realistic situation from the bench to the scanner. When the two outer coils were connected simultaneously, we observed the corotating and counterrotating modes for each peak [25]. We tuned the corotating mode down to 127.75MHz with a capacitance at each leg of 27.9pF and then matched the outer coils to 50Ohms.

2.3 Methods for Evaluation

2.3.1 Simulations

The objective of the simulation was to show whether the new split birdcage coil is a feasible version that utilizes the same phenomena as the 4-ring coil in terms of producing a homogeneous magnetic field for ^{1}H in the center of the coil. Simulated for this study were two different birdcage coils, the 4-ring design and the split design, as shown in figure 2.1, along with a simulated test for various distances between coils in the split design. The new split design dual-tuned birdcage coil in this study was chosen from the 4-ring low-pass low-pass (LP-LP) design and simulated as such where the two outer coils are tuned for ^{1}H and the inner coil is tuned for ^{31}P. The simulated coils were designed to be LP-LP so that the excitation sources could be placed easily and reliably in the simulation (sources could only be directed in the 3 Cartesian directions)

The optimization of the physical parameters of a 4-ring dual-tuned coil has been explored in the past [21, 24, 25]. However, the coils for this experiment are intended for imaging of the adult human thigh. The diameter, length of the inner coil, length of the outer coil, and coil separation (for the split design only) were set at 23.45cm, 20.79cm, 4.51cm, and 0.4cm. The structure of three separated 8-leg birdcages was modeled with consideration of the optimum dimensions found by Duan et al [21].

Simulations were run with a finite difference time domain program, xFDTD (Remcom, State College, PA), to calculate and map the magnetic field. Since the physical dimensions of the ^{31}P coil on each dual-tuned birdcage were the same and each coil was centered on the sampling region, simulations were not run for it. The split birdcage coil used three separate LP coils in a

line. The 4-ring dual-tuned LP-LP birdcage coil uses 4 conducting rings connected with conducting legs that form three individual sections, an inner section and two outer sections. In each case, the outer sections are for ^{1}H imaging (127.72MHz for Hydrogen at 3T) and the inner section is for ^{31}P MRS (51.7MHz for phosphorus at 3T). The mesh was set up to be more than twice the size of the coil with an adaptive mesh that had a cell size of 2.58mm in the region of the coil and 21.66mm far from the coil. Ten cycles were run to make sure that a steady state had been reached and a slice across the x-y or y-z plane was chosen at the same time point from each of the three simulations. The primary mode of a LP or HP birdcage coil has a sinusoidal current distribution around the legs of the coil which produces a rotating magnetic field in the center of the coil. This sinusoidal current wave propagates around the legs as well as a net sinusoidal current wave around the endrings. Rather than tuning simulated capacitors at each leg of the inner birdcage coil, the magnetic field was generated with z-axis directed sinusoidal voltage sources of value 1V placed at the midpoint of each leg of the ^{1}H coils, at a frequency of 127.75MHz and phase shifted to form a sinusoidal current distribution, i.e. 0, 45, 90, 135, 180, 225, 270, and 315 degrees for the 8-leg coil in this study. Capacitances placed on the inner coil were experimentally found on the bench for resonance at 51.7MHz. Each capacitor was 23.0pF for the 8-leg coil. The magnetic field generated around the mid-point of the cycle was analyzed for homogeneity and sensitivity in the xy-plane, or the transverse plane, and the yz-plane, or the coronal plane.

Because the analysis was performed with free space loading, coil losses and tissue loading were not included in the simulation. According to the principle of reciprocity, a transmit coil's B_1 field distribution per unit current is equal to the signal distribution acquired from the same coil for reception. Therefore, a normalized B_1 field will give an equivalent idea of the coil's

sensitivity [44, 45]. Instead of presenting an absolute magnetic field, we normalized the B_1 fields of each coil to their centers in order to reflect the relative B_1 fields of these coils. The normalized magnetic field profile was analyzed and displayed in both the xy-plane (transverse plane) and the yz-plane (coronal plane).

To further understand how the split birdcage coil spacing affects the coil performance, FDTD simulations were run with several different distances between the coils. Distances used included 8mm, 6mm, 4mm, 2mm, and 0.5mm. The results were plotted in figure 2.5.

2.3.2 Experiment

The ^{31}P surface coil was placed on the thigh sized phantom as well as the human thigh so that the ^{31}P coil was positioned on the right side of the right leg. The phantom as well as the human thigh was centered inside of the birdcage coil. All data were acquired by using a GE 3T HDx magnet (GE medical systems, Milwaukee, WI).

For comparison purposes, a dual-tuned surface coil (Clinical MR Solutions LLC., Brookfield, WI, USA) was used for data acquisition, which consists of a single 13cm by 13cm square ^{31}P coil, with 20.5cm by 22.5cm ^{1}H coils on either side with 3.25cm of overlap as seen in figure 2.1. The total length of the surface coil is 41cm and it is flexible so that it can be wrapped around the subject.

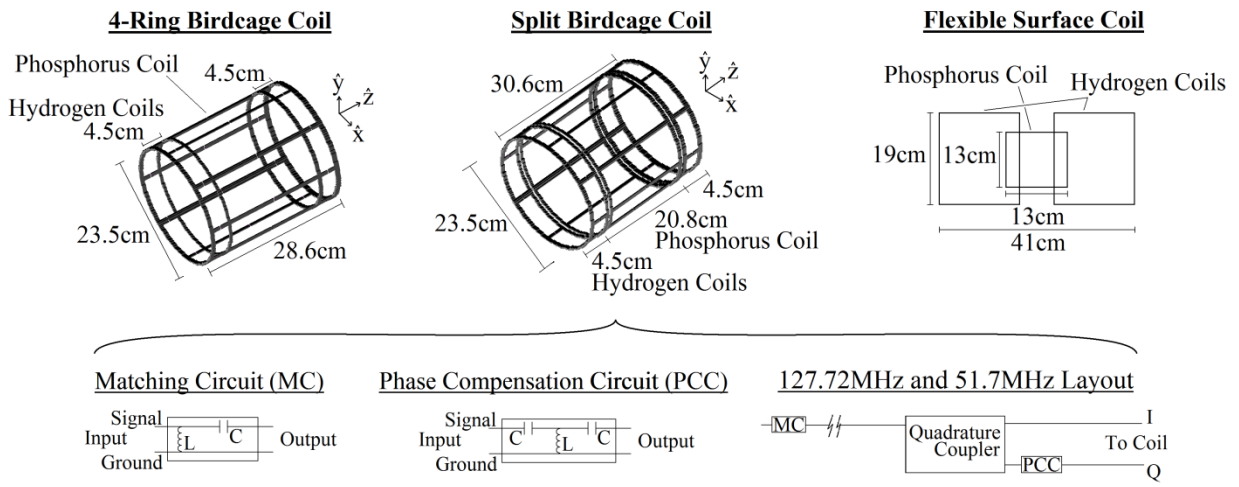

Figure 2.1: Schematic showing, (Top) the 4-ring dual-tuned birdcage coil (Left), the split birdcage coil (Middle), and the flex surface coil (Right) and (Bottom) the network of matching, splitting, and phase shift compensation to the coil. The 4-ring birdcage and the split birdcage were modeled in xFDTD and compared with each other within the simulations for ^{1}H field sensitivity. For the proposed split birdcage coil, the matching circuits used were two component circuits composed of a capacitance and an inductance. The phase shifting circuits were T-shape circuits composed of two capacitors and one inductor.

The protocol for acquisition was first to obtain an anatomical image using a gradient recalled echo (GRE) sequence, followed by a 7x7 free induction decay chemical shift imaging (FID-CSI) sequence. The FID-CSI data were acquired after both auto- and manual-shimming to maximize signal intensity and peak shape.

Parameters for anatomical image acquisition for both the split birdcage coil and the MNS surface coil while imaging the phantom consist of a repetition time (TR) of 350ms, an echo time (TE) of 10ms, a flip angle (FA) of 90 degrees, a field of view (FOV) of 18cm, a slice thickness (STH) of 20mm, and frequency and phase resolution of 256x256. While imaging the human leg, the parameters were the same for the flex coil, but the parameters for the split birdcage coil were

TR of 100ms, TE of 7ms, FA of 90 degrees, FOV of 18cm, and STH of 20mm. The magnitude for a central axial slice was recorded. The FID-CSI data for both the split birdcage coil and the MNS surface coil had these parameters: a TR of 3000ms, a FA of 90 degrees, a FOV of 18cm, a STH of 20mm, and displayed grid dimensions of 7x7. Four excitations were acquired resulting in a scan duration of 10 minutes.

In this study a main objective is to use the split birdcage coil to measure oxidative metabolism in skeletal muscles of a human thigh. The human subject dataset was acquired from a volunteer with a protocol approved by the institutional review board of the University of Georgia. The MNS surface coil was positioned such that the ^{31}P coil lay at the midpoint of the thigh offset from the top of the thigh towards the vastus lateralis muscle. The ^{31}P coil of the split birdcage coil was centered on the midpoint of the thigh. The FID CSI spectral voxels were approximately isotropic cubes measuring 2x2.25x2.25cm.

2.3.3 Data processing

All data processing was done with MATLAB (The MathWorks, Natick, MA). From the simulated magnetic field map, a ROI was selected within the boundaries of the coil. For the axial view and the coronal view, the ROI is approximately a 6.33cm x 6.33cm square, about one third the diameter of the phantom used in the experiment. A measure of the ^{1}H field sensitivity was displayed with the normalized field maps from the simulations inside the ROI.

The experimental raw FID signal was loaded into MATLAB and then reconstructed with a two dimensional fast Fourier transform of the entire FOV in combination with one dimensional processing to add a line broadening of 3Hz that was accomplished by taking each spectrum and doing an inverse fast Fourier transform, multiplying the resulting FID-like signal by the Gaussian

smoothing function and then fast Fourier transforming back to the frequency domain. The SNR was calculated voxelwise for the ^{31}P signal FID-CSI grids by building noise vectors from the first 600 data points from each spectrum of 2048 data points. The dominant ^{31}P peak (PCr) from each spectrum was about 400 data points away from the noise vector. The maximum value from each spectrum was divided by the standard deviation of that spectrum's noise vector to obtain the SNR.

2.4 Results

2.4.1 Homogeneity of the ^{1}H coil

Figure 2.2 shows the normalized field maps with respect to the center of its ROI obtained from simulation for a central axial slice (A and C) and a central coronal slice (B and D) for the 4-ring coil and the split birdcage coil. Also in figure 2.2, the y-, z-, and x-directed magnetic field profiles across the ROI are shown for the simulations (E, F, and G). Because a constant (1V) voltage source was used for each coil, the coils have the same dimension, and equivalently the same coil resistance, the field maps after normalization can be regarded as ones generated by unit current sources. The sensitivity of each coil configuration can be seen from the rate at which the field falls off. For the axial slice of the 4-ring coil, a region of homogeneity that is within 5% of falloff from the center is outlined by a black border as seen in figure 2A. The area of this region is 94.5% of the ROI. The axial slice of the split birdcage coil has a smaller region of homogeneity that is 47.0% of the ROI by area with the same 5% of falloff from the center field criteria, as shown in figure 2C. For the coronal slice, the 4-ring coil has a larger region of

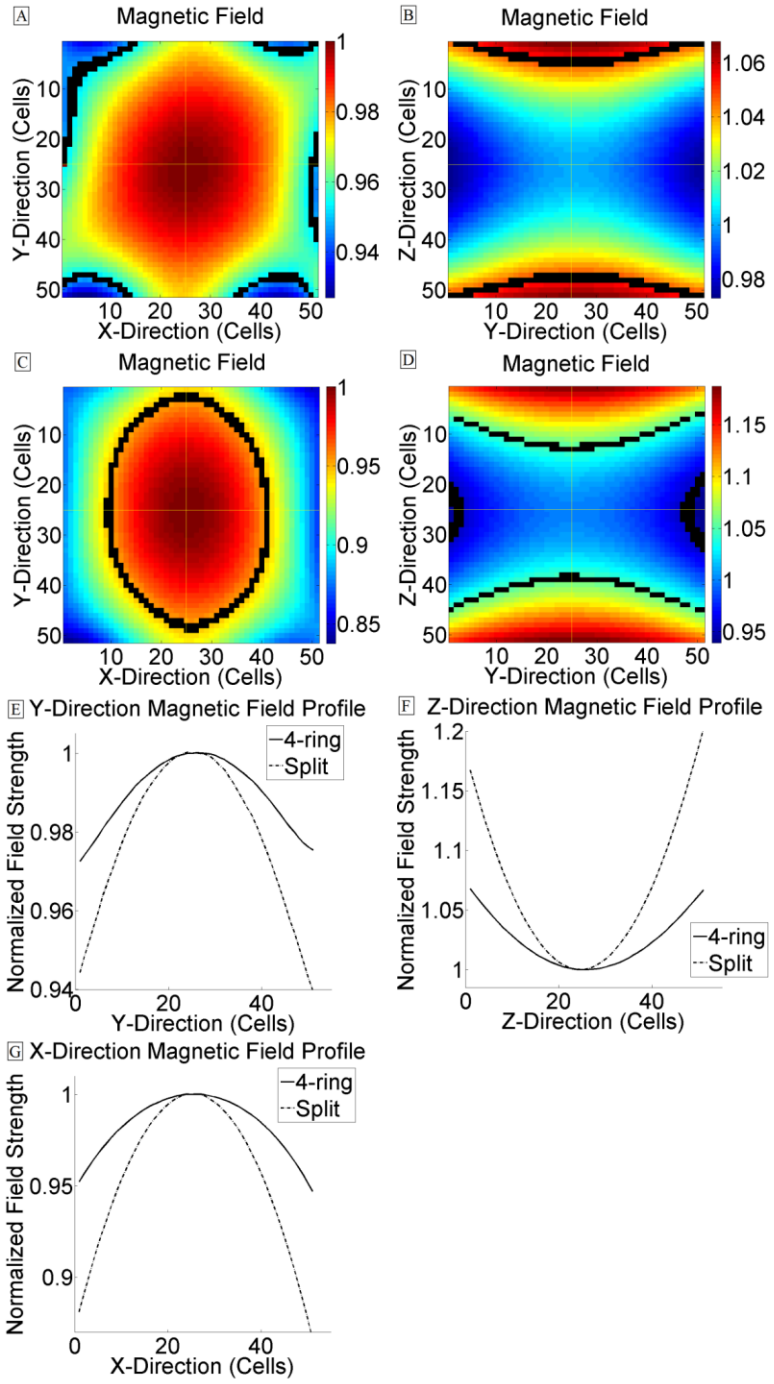

Figure *2.2*: Simulation results from the 4-ring birdcage coil are displayed for an axial slice (A) and a coronal slice (B), followed by simulation results from the split birdcage coil for an axial slice (C) and a coronal slice (D). A, B, C, and D show the magnitude of the normalized field with respect to the center of the ROI; while E, F, and G show the normalized magnetic field profile across the coil center in the y-, z-, and x-directions for the two coils. The x-axes are displayed in units of cells (0.21 cm/cell). The 4-ring coil has an axial magnetic field that is more homogeneous across the ROI with a larger area within 5% deviation, while the split birdcage coil has a smaller area. The thick black line on graphs (A), (B), (C), and (D) outlines the border of a

deviation of 5% from the field at the center of the ROI. For the axial slice, the 5% line encompasses 94.5% and 47.0% of the ROI for the 4-ring coil and the split birdcage coil respectively. For the coronal slice, the 5% line encompasses 93.1% and 61.9% for the 4-ring coil and the split birdcage coil respectively. Also, a consistent trend can be seen in the gentle rise to the center of the magnetic field profile in the transverse plane and a smooth fall to the center along the z-axis directed profiles of the coronal slices (F).

homogeneity (93.1%, shown in figure 2B) than the split birdcage coil (61.9%, shown in figure 2B) by area of the ROI. The magnetic field profiles along x-, y-, and z-direction, shown in figure 2.2E, 2.2F, and 2.2G, show that the field rises and falls in a smooth curve passing through the center of the normalized field.

Figure 2.5 shows the relationship between the spacing of the split coils and the mean magnetic field inside of the ROI. The induced field is inversely proportional to the distance between the coils. This is to show the efficiency of the coil to coil coupling with a fixed input power.

2.4.2 Homogeneity of ^{31}P Signal

To compare the homogeneity, the data are displayed as an overlap of the FID-CSI grid on top of the anatomical image. Figure 2.3 displays the experimental results acquired from the phantom, with its magnitude of the spectral signal for each voxel in the 7x7 grid overlapped on the anatomical image. In figure 2.3, it was observed from the two 100mM KH_2PO_4 phantom scans that the depth to which the surface coil can acquire ^{31}P signal is less than half of the 18cm diameter phantom. The split birdcage coil, however, obtained signal uniformly from every voxel

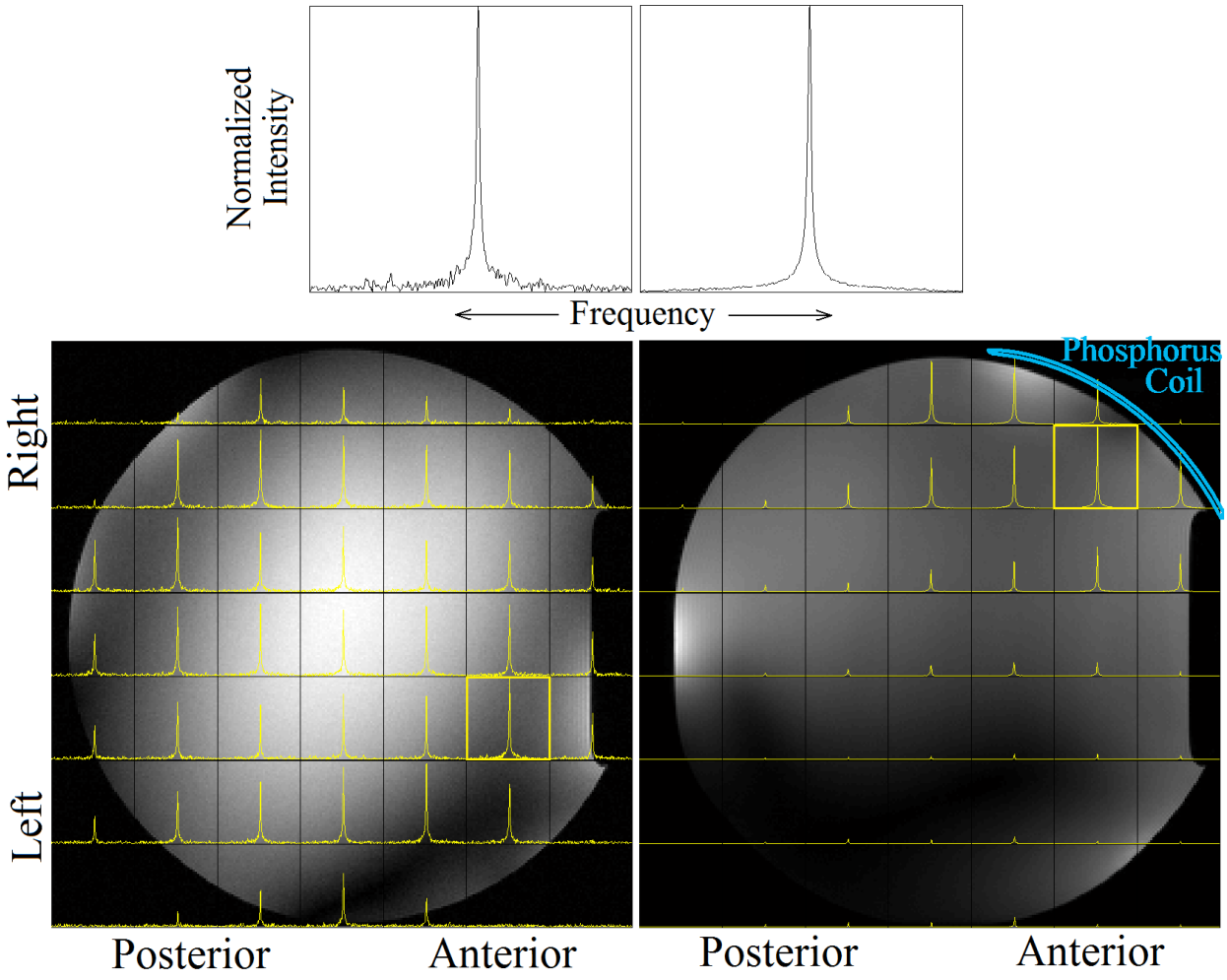

Figure 2.3: This compares side by side the overlapped FID-CSI grid on top of the anatomical image for a 100 mM KH_2PO_4 phantom for both the split coil (Left) and the flex surface coil (Right). Note that the flex surface coil is over the top right of this image. The spectral peaks were acquired with the same digital, analog, and transmit gains. The ^{31}P voxel with the highest intensity peak (shown in the highlighted box) was selected and expanded above.

across the phantom including the voxel in the very center of the grid. As a comparison, the SNR was calculated at each voxel for both coil datasets and displayed in table 2.1, which is organized in a way that directly correlates the position of the FID-CSI voxel and the position of the

Table 2.1: presents numeric values for the SNR from each block in the corresponding FID-CSI grid from figure 2.3. SNR table for A) the split birdcage coil and B) the flex surface coil, physically located at the top right of the FOV of the phantom.

A)

8.59	15.39	66.69	44.55	40.80	26.25	9.49
13.20	96.52	100.62	94.62	63.95	65.38	64.34
82.68	102.83	102.70	90.69	70.01	83.77	53.47
72.19	106.10	99.89	102.80	112.40	119.01	69.23
44.08	90.39	86.74	75.68	83.10	89.29	56.83
44.14	76.64	97.34	111.48	112.39	83.92	6.48
3.87	21.17	56.94	68.95	46.96	6.53	5.51

B)

27.51	14.43	163.88	285.66	271.23	241.60	46.61
40.76	88.07	242.05	263.93	280.58	298.63	262.25
46.75	72.96	70.98	175.22	218.11	279.21	254.76
6.92	33.32	70.78	106.86	137.18	116.19	51.86
6.07	19.64	29.89	37.67	67.96	63.92	47.42
8.77	19.35	53.43	45.07	73.02	20.41	34.18
7.67	28.41	46.51	48.89	94.92	32.13	22.73

calculated SNR. For the surface coil, the SNR at areas close to the coil was ~275 and dropped off quickly with the distance from the coil. For the split birdcage coil, there were many voxels within the phantom that gave a SNR of 100. The best SNR value for the split birdcage was 119.01 while the best SNR for the surface coil was 298.63.

The comparison between the split birdcage and the surface coil for the human thigh is shown in figure 2.4. This display combined with the spatial encoding of the FID-CSI allows for the correlation of signal to a localized region, in particular, to a localized muscle anywhere from the vastus lateralis on the surface of the leg to other muscles deeper in the tissue. The surface

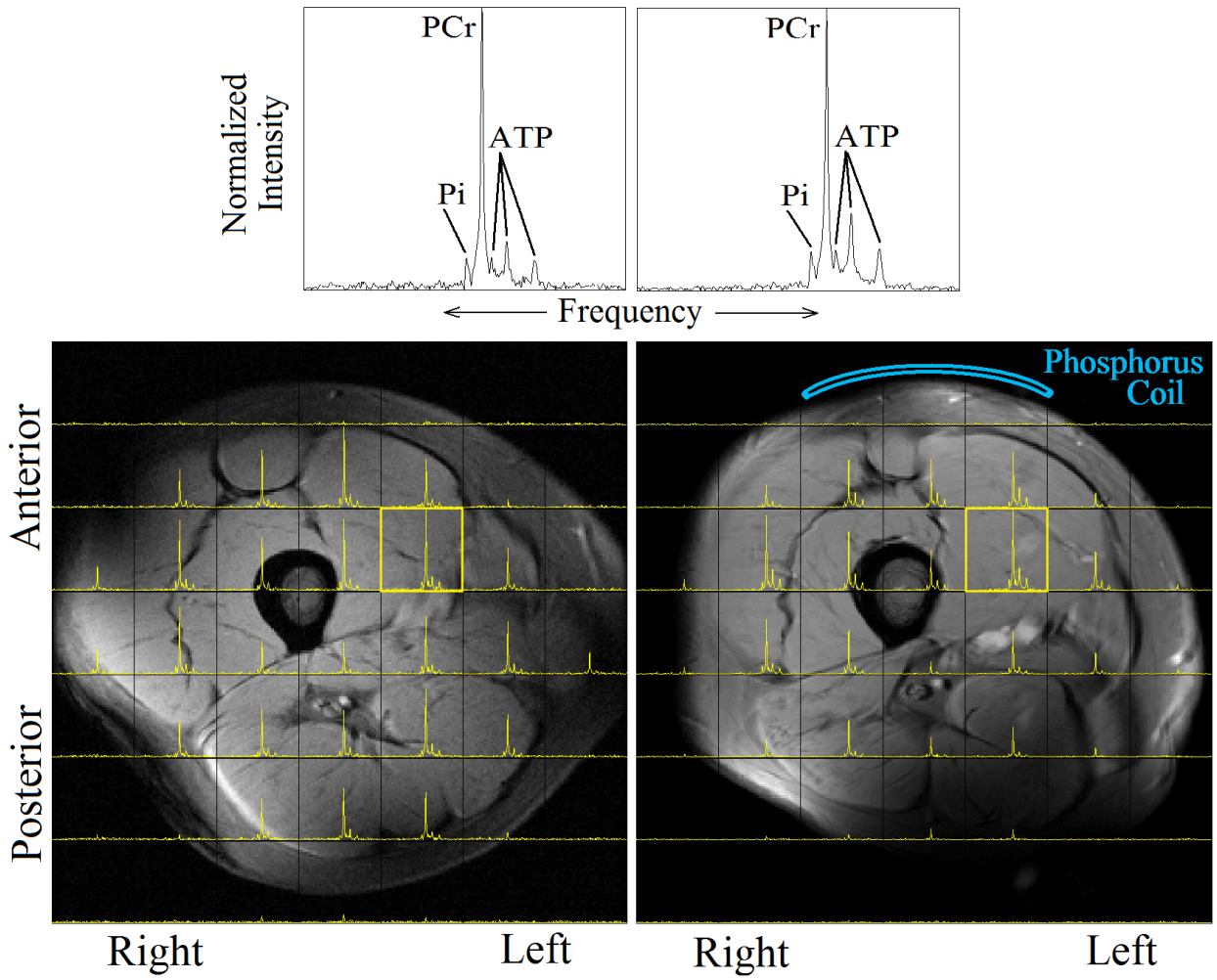

Figure 2.4*:* Displayed in this figure are the overlapped FID-CSI on top of an anatomical image of the human thigh for the split coil (Left) and the flex surface coil (Right). Since the only source for PCr is the muscle, the partial volume effect can be seen at the boundaries of muscle to fat, bone, and blood vessels. There is reduced signal intensity when only part of the voxel is filled with signal producing sample. The ^{31}P voxel with the highest intensity PCr peak (shown in the highlighted box) was selected and an expanded view is shown above.

coil, when placed around the thigh orients the ^{31}P coil slightly off center toward the vastas lateralis muscle on top of the leg. The PCr peaks are visible for the surface coil at grid positions close to the coil. For the split birdcage, a PCr peak appears at every grid position that sits on a

Table 2.2: presents numeric values for the SNR from each block in the corresponding FID-CSI grid from figure 2.4. SNR table for A) the split birdcage coil and B) the flex surface coil, physically located on top of the thigh.

A)

4.99	8.83	5.58	7.38	8.60	8.32	6.10
6.89	82.34	153.19	169.40	114.39	15.12	5.70
51.23	170.17	117.48	139.11	146.47	86.33	6.58
77.28	152.55	71.41	66.09	138.29	159.28	53.94
7.42	86.28	113.00	109.51	174.45	112.48	5.71
11.64	12.74	94.41	106.14	137.96	13.15	6.39
5.42	7.10	14.57	17.69	10.88	6.29	4.32

B)

5.13	10.90	5.29	5.56	4.69	7.70	4.91
7.95	74.60	176.93	161.37	192.78	53.10	7.12
34.58	239.57	205.40	121.45	305.73	124.68	23.36
17.75	165.51	213.06	40.22	143.93	53.69	19.36
13.39	54.92	120.61	68.34	91.37	37.29	5.99
4.55	14.98	22.45	37.25	35.06	5.89	6.61
7.92	8.76	8.70	7.46	5.76	5.47	7.34

piece of muscle. Quantitatively, table 2.2 displays the calculated SNR from each voxel in the 7x7 FID-CSI grids. The highest SNR from the split birdcage is 174.45 while that of the surface coil is 305.73.

2.5 Discussion

Previously, it has been shown that for a typical two-ring birdcage, the region of good homogeneity extends almost to the coil legs in the axial slice and almost to the end-rings in the coronal slice [33]. In principle, the split birdcage design utilizes inductive coupling between the outer coils and the inner coil in order to produce the same effect of corotating and

counterrotating modes as the 4-ring coil design without the trouble of iterative tuning. This has been shown to produce a rotating magnetic field in the center of the coil greater than the field produced by the brute force method of using two ^{1}H coils [21, 25]. Also, it should be noted that when simulating the ^{1}H coils alone, there was a distinct pattern visible from interference between the two ^{1}H coils. This pattern was probably still there to some extent in both the other simulations, but because field strength was an order of magnitude greater than that of the ^{1}H coils alone, the pattern was not seen.

The comparison coil, the surface coil, is designed to surround the ROI with two ^{1}H surface coils parallel to each other making up slightly for the well known disadvantages of surface coils, like its inability to acquire good signal at a distance away from the coil. This particular point is a textbook rule. However, the reason that this disadvantage is most often overlooked boils down to the fact that surface coils are very easy to reproduce reliably. Volume coils on the other hand are more difficult because they bring more complexity by way of tuning. Dual-tuned volume coils even more so. A volume coil, that is easy to reproduce, and effective at multinuclear spectroscopy has the advantage over the surface coil counterpart for all applications except attempting to acquire signal right on the surface of a tissue.

For the split birdcage coil, the ability for the two outer coils to acquire signal from a central location far from either ^{1}H coil is necessary but does not need to be optimized for the objective of the coil is multinuclear spectroscopy. Using a split birdcage spacing of 4 mm and comparing it to the 4-ring coil, the mean field strength in the center is half that of the 4-ring coil. However, since the mean field strength depends inversely in an exponential manner, simply

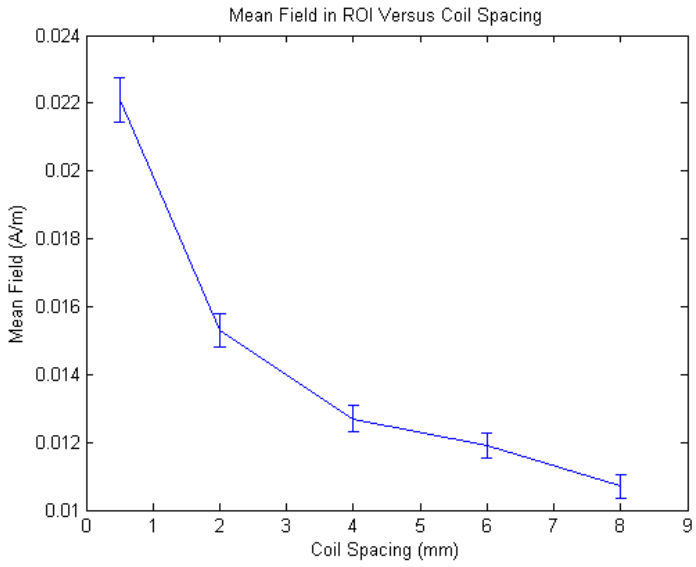

Figure 2.5: Simulations of the split birdcage coil were run to show the magnetic field inside of a ROI against the spacing between the coils. The field generated is proportional to the coupling between the coils and that is determined by the distance between the endrings of the ^{31}P coil and the ^{1}H coils. The spacing between the coils, in this study, was 4 mm.

decreasing the distance of the spacing from 4 mm to 2 mm or even 1 mm, the mean field strength would approach that of the 4-ring coil in a non linear fashion. So long as the coils are not directly connected, tuning is simplified by breaking the split birdcage coil into three coils.

Simply by visual comparison of the images acquired with both the flex surface coil and the split birdcage coil it's apparent that each coil has some dark spots. The split birdcage has a dark spot in the same pattern that the ^{1}H coil simulation showed which means perhaps the image is more susceptible to that interference inside of the scanner. The surface coil has a large dark spot because the material to be imaged is too big for the flexible coil to fit around and therefore a dark spot is left. Neither of these dark spots hinders the function of the coils though. The SNR for the image is comparable and, in the human thigh scans, all of the anatomy can be seen. That

is what is required in order to map back a particular ^{31}P spectrum to some localized region of the tissue. As seen in figure 2.3 and 2.4, the ^{31}P signal drops off rather quickly for the flex coil on the phantom and slightly less quickly for the human thigh scan. The split birdcage on the other hand maintains a uniform ^{31}P signal across the subject, phantom or human thigh. By comparing the highest SNR from a voxel for the phantom scans for the surface coil and the split birdcage coil, seen in table 2.1, it appears that the SNR from the split birdcage is less than half that of the surface coil. However, it also appears that the high SNR value continues to the center of the phantom for the split birdcage coil while the high SNR for the surface coil is limited to the area close to the coil. The voxel with the highest SNR from figure 2.3 is analyzed to show that the SNR value for the split birdcage coil is 119.01 vs 298.63 for the surface coil.

The results from the human thigh dataset were consistent with that of the phantom experiments. The peak SNR value for the birdcage coil, 174.45 was greater than half of the peak SNR value for the surface coil, 305.73, and a good SNR was obtained for all voxels containing skeletal muscle.

Quantitatively speaking, table 2.1 and 2.2 convey all of the numerical results for ^{31}P SNR calculations. They show that the birdcage in fact has a smaller variation in ^{31}P peak intensity and therefore a more homogeneous B_1 magnetic field in the axial slice. This is expected based on the fact that these are textbook phenomena. However, this does answer the question of whether or not this new design of birdcage coil, the split design birdcage, is efficacious in acquiring signal for imaging and MNS like previous 4-ring birdcage coils while at the same time exhibiting ease of construction and tuning.

Another method for finding homogeneity is to highlight a region that satisfies a criterion such as mean variation is less than 5% or 10%. This method shows the region of good

homogeneity [21, 36, 37] and was the method used to display field homogeneity and coil sensitivity from figure 2.2.

This coil has not been attempted before. It reduces practical difficulties inherent in dual-tuned birdcage coils such as complexity in multiple components, capacitor symmetry, iterations of tuning and matching, etc. for tuning the coil to 51.7MHz and 127.75MHz respectively for ^{31}P and ^{1}H and matching the coil to 50Ohms. On the bench, anything that is directly connected to the coil will affect the tuning. Having the coils separated means that there are no components in parallel with the individual ^{31}P coil and ^{1}H coils, and individually, the resonant modes produced are the pure modes for a birdcage of each size. Capacitor symmetry is very important when tuning, and additional connected components can create unexpected resonant modes as well as interfere with the symmetry.

This study was designed to introduce the new split birdcage coil while simultaneously evaluating it for eventual performance acquiring localized multinuclear signal from the skeletal muscle of patients that might or might not have a large layer of subcutaneous fat surrounding the muscle. This has been a concern with the available commercial surface coils that would not be able to detect signal from deep inside tissue.

The preliminary simulations compared the design to a previously constructed 4-ring coil and through analysis, it was determined that the split birdcage coil would in fact operate under the same principles as the 4-ring coil though it would generate a slightly weaker magnetic field homogeneity and coil sensitivity in the center of the coil. The coil was tested against a commercially available dual-tuned flexible surface coil experimentally by acquiring both ^{1}H signal and ^{31}P spectra from a large 18cm diameter phantom and a normal, healthy human thigh. The results showed that, as predicted, the split birdcage coil, because it is a volume coil, gave a

more uniform ^{31}P signal from both the phantom and the human subject making it a much better choice for acquiring and localizing signal from a particular muscle in the tissue. This is a useful result because of the ease with which the split birdcage coil can be constructed. Having the three coils spaced apart instead of directly connected cut back the iterative tuning process and allowed for individual matching for each section without interference to the other coils. The future of this research will be to consider human subjects with large layers of subcutaneous fat [18] which act as a buffer between the muscle and the coil. The more fat there is, the greater the distance would be to a surface coil, and the weaker that signal would be. This would not be the case for the split birdcage coil.

In conclusion, a new dual-tuned split birdcage coil was developed and compared to an existing 4-ring birdcage coil and a flex surface coil with simulations and experiments, respectively. The new design of birdcage coil greatly reduced the number of iterations of tuning and matching by taking away the direct connection between the outer ^{1}H coils and the inner ^{31}P coil. This makes it possible to easily build the coil and to adjust the tuning or matching before a scan. It was found that the ^{1}H coil sensitivity of the split birdcage coil was slightly less than that of the 4-ring coil. Also, the ^{31}P homogeneity of the split birdcage coil was much better than the flex coil.

CHAPTER 3

A BASELINE STUDY WITH THE SPLIT BIRDCAGE COIL

In this chapter, I present a study that was conducted to lay out a baseline of data for our newly developed dual-tuned Hydrogen/Phosphorus ($^{1}H/^{31}P$) birdcage coil, referred to as split birdcage coil, introduced in the previous chapter, and evaluate its performance across a ten-subject trial. Subjects for this study were selected from healthy individuals with varying body mass indices (BMI). Data were collected with both the split birdcage coil and a commercial dual-tuned surface coil, and analyzed for the normalized phosphocreatine (PCr) peak signal to noise ratio (SNR). A segmentation routine was run on anatomical images and percentages of muscle for each segment, or block, were compared to the free induction decay chemical shift imaging (FID CSI) spectral grid ^{31}P signal from the corresponding block. The results showed that there was a linear relationship between the percentage of muscle in a given region and the PCr SNR for the split birdcage coil.

3.1 Introduction to the Focus of this Study

Multinuclear Spectroscopy (MNS) has become a widely used tool for the study of oxidative metabolism indices, such as kinetic changes in phosphocreatine (PCr). The rate of PCr recovery is a good *in vivo* indicator of oxidative capacity [9]. When considering an experiment of this nature, points of concern include coil sensitivity, signal to noise ratio (SNR), localization to a specific skeletal muscle, and speed of signal acquisition [9, 11-13, 17]. With the exception of

speed of signal acquisition, all of these concerns revolve around the radio frequency (RF) transmit/receive coil. Volume coils for this purpose have become more and more prominent over the years. A dual-tuned birdcage coil has many advantages over a dual-tuned surface coil. A birdcage coil would not have SNR as high as the surface coil when targeting a point next to the surface coil, but a birdcage coil would be able to target anywhere within the field of view (FOV) inside of the coil. This is a big advantage when a subject has a large layer of subcutaneous fat surrounding the tissue to be scanned.

Many styles of dual-tuned birdcage coils have been experimented with where each has its own advantages and disadvantages [11, 12, 21-34]. The split birdcage coil was developed for the purpose of easier tuning when it comes to building the coil. It was modeled after a 4-ring design [25] which positions the multinuclear coil directly around the target tissue and keeps a pair of ^{1}H coils symmetrically on a cylinder on either side of the center coil. The 4-ring design has all three of these coils connected so that at each connection there is an endring that is shared. However, the split birdcage separates these coils so that no endring is shared.

In this study, a baseline of data was acquired with the new split birdcage coil and the data were analyzed with a segmentation method that relates the ^{31}P spectral signal to the specific region from which the spectral signal came.

3.2 Methods

3.2.1 Protocol

A homemade dual-tuned split birdcage coil and a commercial flexible dual-tuned surface coil (Clinical MR Solutions LLC., Brookfield, WI, USA) were used to scan a population of ten healthy subjects with a GE 3 T HDx magnet (GE Medical Systems, Milwaukee, WI). The ten

healthy subjects were recruited on a volunteer basis for this institution review board (IRB) approved study and were asked to participate for one hour of scanning. Subjects had varying degrees of subcutaneous fat surrounding the muscles of the thigh, 4 were male and 6 were female, and ranged in age from 23 years old to 48 years old. A protocol timed to one hour was used to scan a localizer, an anatomical image, and a 7x7 chemical shift imaging free induction decay (FID CSI) spectral grid for both the split birdcage coil and the flex coil. The targeted skeletal muscles were those of the thigh. The split birdcage coil was designed to fit this anatomy and be able to acquire a good SNR across the entire field of view (FOV). The commercial flex coil has been used in previous studies [15-17] to acquire both anatomical and spectroscopic data from the thigh. In the scanner, a gradient recalled echo (GRE) sequence was used with the split birdcage coil to acquire an anatomical image with an echo time (TE) of 7 ms, a repetition time (TR) of 100 ms, a flip angle (FA) of 90 degrees, a bandwidth (BW) or 15.63 Hz, a matrix size of 256 by 256, a FOV of 18 cm, a slice thickness (STH) of 20 mm, and a number of excitations (NEX) of 16. For the flex coil, a GRE sequence was used with a TE of 10 ms, a TR of 350 ms, a FA of 90 degrees, a BW of 15.63 Hz, a matrix size of 256 by 256, a FOV of 18 cm, a STH of 20 mm, and a NEX of 4. Within the protocol, both automatic and manual shimming was performed based on a proton spectroscopy (Press CSI) sequence. The shimming gradient values were then carried over to the ^{31}P FID CSI scan. Values for the FID CSI used for both coils include a TR of 3 sec, a FA of 90 degrees, a grid size of 7 by 7, a FOV of 18 cm, a STH of 20 mm, and a NEX of 4.

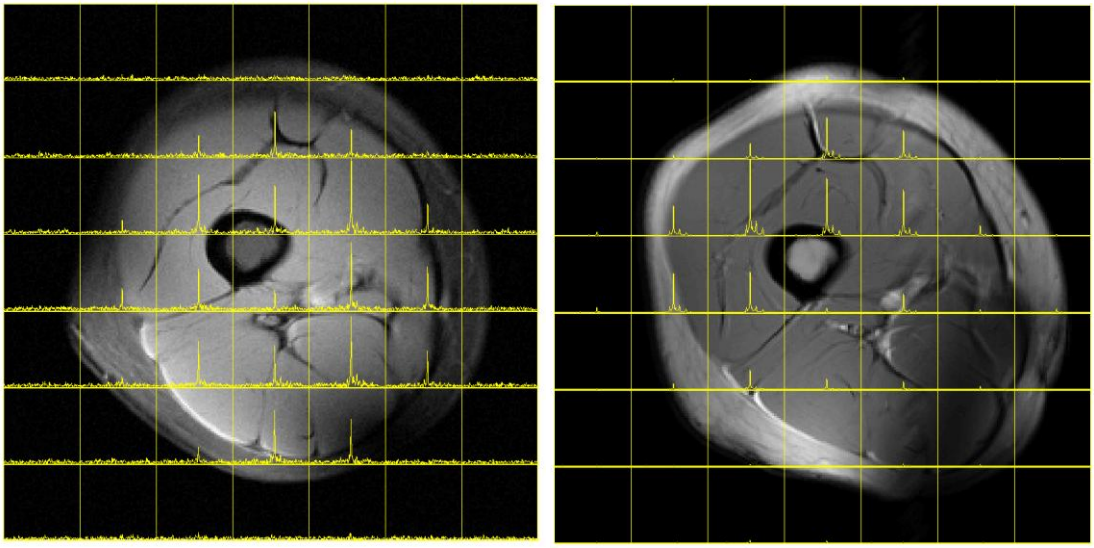

Figure 3.1**:** Shown in this figure are the anatomical images with overlapped FID CSI grids for the split birdcage coil (Left) and the flex coil (Right).

3.2.2 Data Analysis

The raw FID-CSI data gathered from this experiment was loaded into MATLAB (The MathWorks, Natick, MA) and the spectroscopy was reconstructed with a two dimensional fast Fourier transform, followed by a line broadening of 3 Hz to the spectroscopic data. Then the 7x7 spectral grid was overlapped with the anatomical image. Though the idea of muscle/fat segmentation has been discussed earlier [46], in order to quantitatively correlate the spectroscopic signal to the specific region on the anatomical image, the anatomical image was segmented and a percentage of muscle for each grid position was calculated with MATLAB. To correct for variations in signal intensity across the anatomical image, the signal across each grid block was analyzed and every voxel within 3 standard deviations of a selected ROI mean for each grid block was included in the percentage of muscle for that block. The range of 3 standard

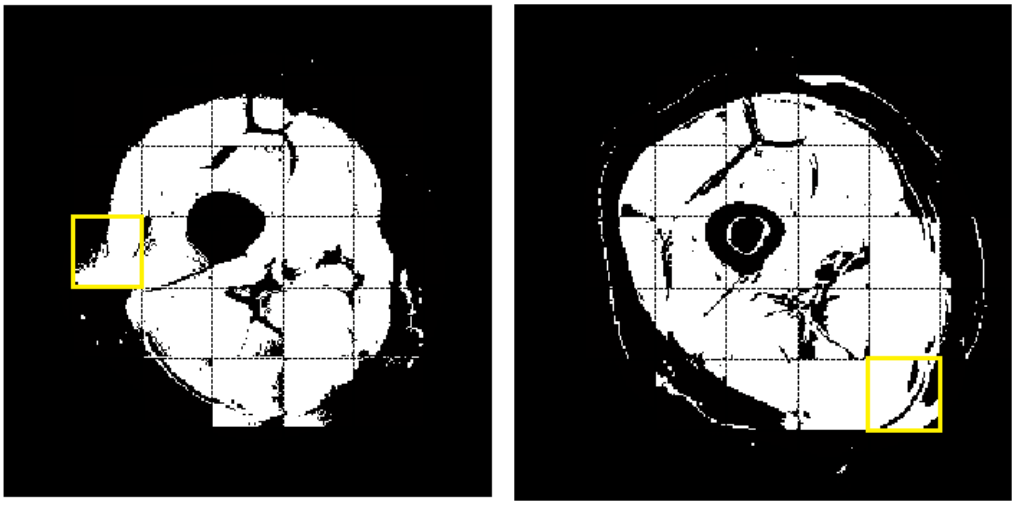

Figure 3.2: The result of segmentation is shown in this figure as the anatomical images are divided into a 7x7 grid producing 49 separate regions that muscle can be chosen from. The image acquired from the split birdcage coil is shown on the Left and that of the flex coil is shown on the Right. The highlighted blocks represent sections where the anatomical image signal intensity is very similar between muscle and fat. In these blocks, the muscle selection breaks down.

deviations was chosen because it gave the best selection of muscle. The variation in the signal intensity across the FOV was such that selecting muscle in the range of 2 standard deviations or less did not select all of the muscle in each of the blocks. A range greater than 3 standard deviations would have over selected the muscle, combining blood vessels, fat, and connective tissue with the muscle. The size of each block was 37 x 37 voxels, but with a matrix size of 256 x 256, 3 empty voxels were added on both the bottom, as rows, and the right side, as columns, of the FOV. The number of voxels in each 37 x 37 block that contains muscle is simply calculated by multiplying the percentage of muscle in a block by 1369. The data are displayed in terms of percentage so that future measurements that might not start with 256 x 256 FOV matrix points can be compared.

Numerically, the SNR for each grid block was normalized according to the subjects maximum SNR. A comparison was made between the ten subjects with these normalized SNR values.

3.3 Results

One of the subjects was chosen to have displayed in figure 3.1 the anatomical image with an overlapped 7x7 FID CSI grid for both the split birdcage and the flex coils. Figure 3.2 shows the pattern for segmentation, with a 7x7 grid exactly matching the grid obtained from ^{31}P spectroscopy. The process of segmenting the anatomical image is done to obtain a percentage of muscle for each grid block based on the signal intensity at each point. The general variation in signal intensity across the FOV makes it impossible to select only the muscle from the image. Therefore, segmentation that focuses on a smaller section at a time reduces the signal intensity variation that occurs across the entire FOV to a more manageable variation that occurs across a single grid block. This allows for a more accurate selection of muscle across the whole FOV. The percentage of muscle is calculated for each grid block and correlated to the normalized ^{31}P PCr SNR for the corresponding grid block and displayed in the plots for the split birdcage and the flex coils. Figure 3.3 shows the plots for the split birdcage coil and the flex coil for one of the subjects. The split birdcage coil data as well as the flex coil data are fit with a linear trend line.

The split birdcage plot has a linear relationship and a best fit line was applied to the data with a slope of 0.0074 and a y-intercept of 0.0706. The R^2 value was 0.9003. The flex coil plot shows that there is not a linear relationship between the percentage of muscle in a given grid block and the ^{31}P signal intensity from the same grid block across the leg. The applied linear trend line has a slope of 0.0041, a y-intercept of 0.474, and a R^2 value of 0.3536. The maximum

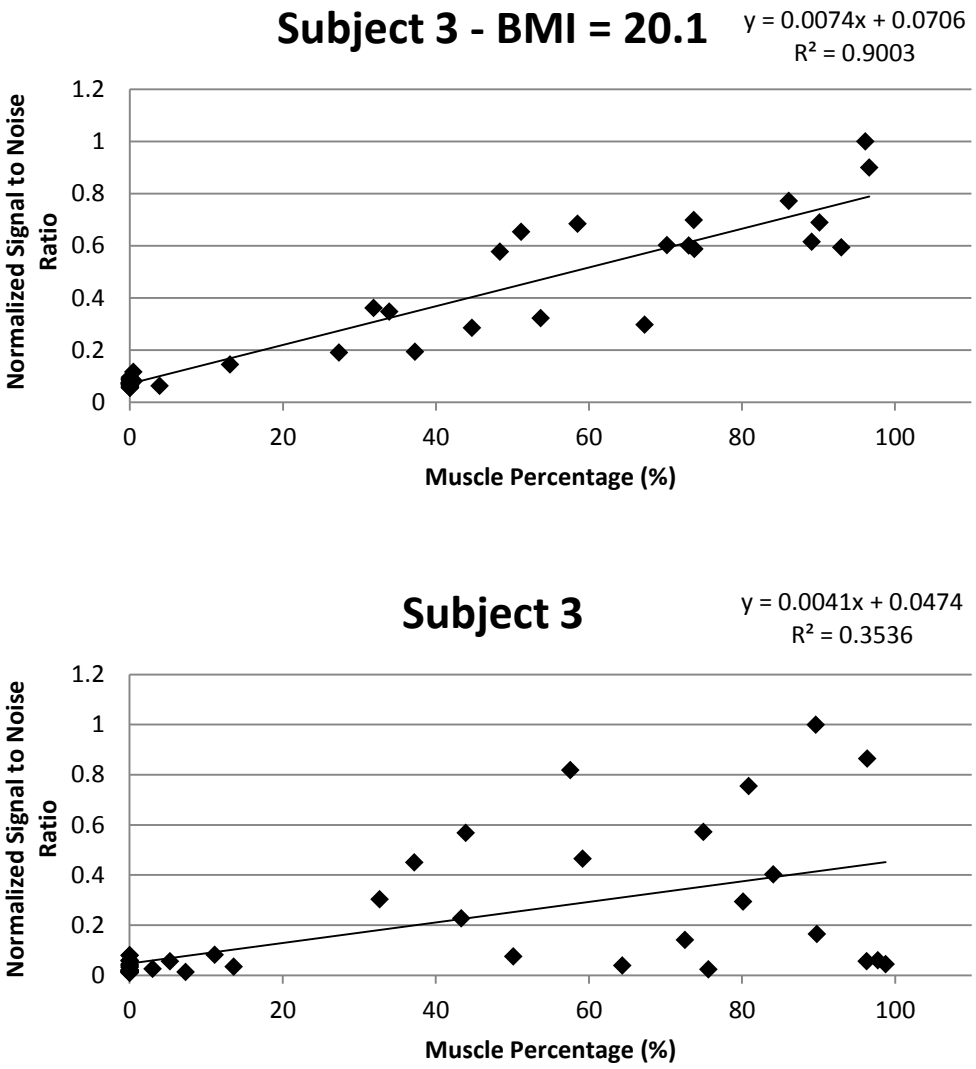

Figure 3.3: These two plots show the normalized SNR of the PCr peaks contained in each grid block of the FID CSI scan. They are correlated with the percentage of muscle within the corresponding grid block as obtained from the segmentation method. The Top plot shows the data from the split birdcage coil with a linear fit. The equation of the line and R^2 value are displayed in the upper right hand corner of the plot. The Bottom plot shows data from the flex coil displayed in the same manner. The data falls within a triangular region which shows that the homogeneity of the flex coil is poor.

SNR comes from a block with 89.6 % muscle while higher percentage blocks give much less signal simply because they are farther from the flex coil. The bottom plot of figure 3.3 shows this trend. These plots were generated for each of the ten subjects and a linear trend line was applied to each of the plots. Figure 3.4 displays the ten trend lines as they appear on the normalized SNR plots. Table 3.1 corresponds to figure 3.4 to show the values for the trend lines and corresponding subject's body mass index (BMI). The BMI is calculated by taking a person's mass in kilograms and dividing by the square of their height in meters. The BMI of a person is a very simple value for whether that person is underweight, has a normal weight, is overweight, or is obese. Typically, a person is underweight with a score less than or equal to 18.4, normal weight with a score between 18.5 and 24.9, overweight with a score between 25 and 29.9, and obese with a score greater than or equal to 30. In this study, 5 subjects are considered to have normal weight, 4 are considered overweight, and 1 is considered to be obese.

3.4 Discussion

Acquiring a baseline of data from the split birdcage coil was the primary goal of this work so that future results could be compared and held to such a standard. The data gathered support the notions that the split birdcage coil is a better tool for spectroscopic analysis of PCr, across the entire FOV of the tissue that is being targeted, over the dual-tuned flex coil; and that the signal acquired from each grid block has a linear relationship with the amount of muscle within the same block.

With the example subject data displayed in figures 3.1, 3.2, and 3.3, it can be seen that prominent PCr peaks exist in every block that contains muscle where as only blocks close to the flex coil clearly show PCr peaks. To correlate this spectroscopic signal to the tissue content of

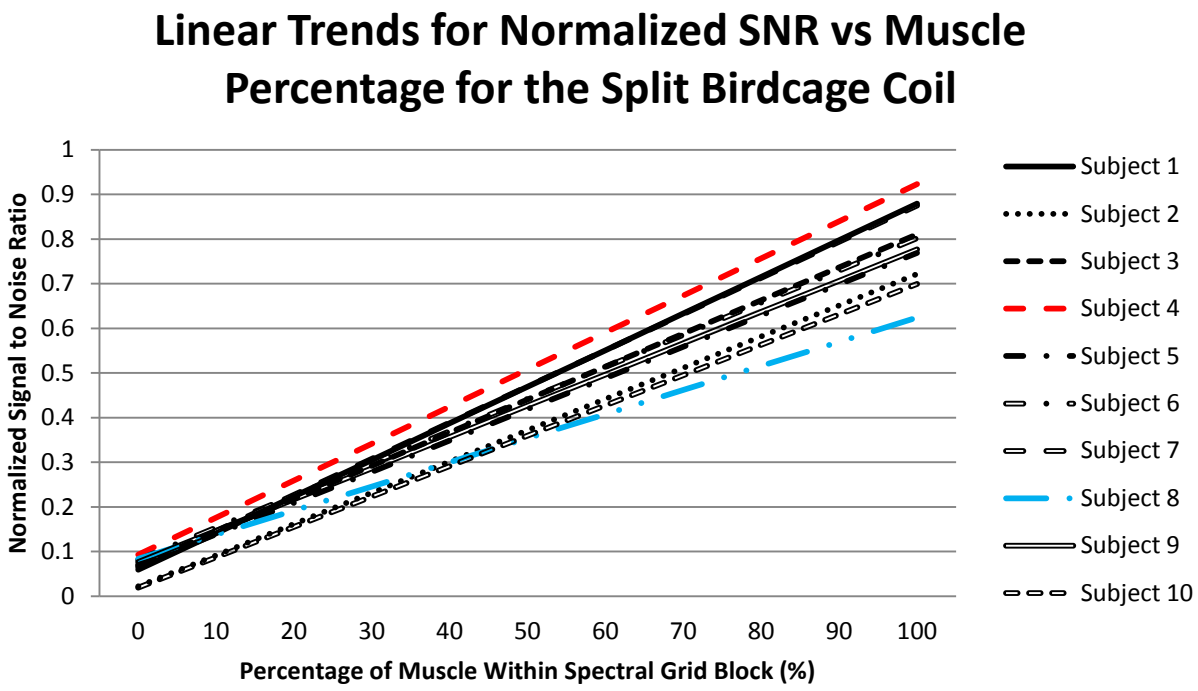

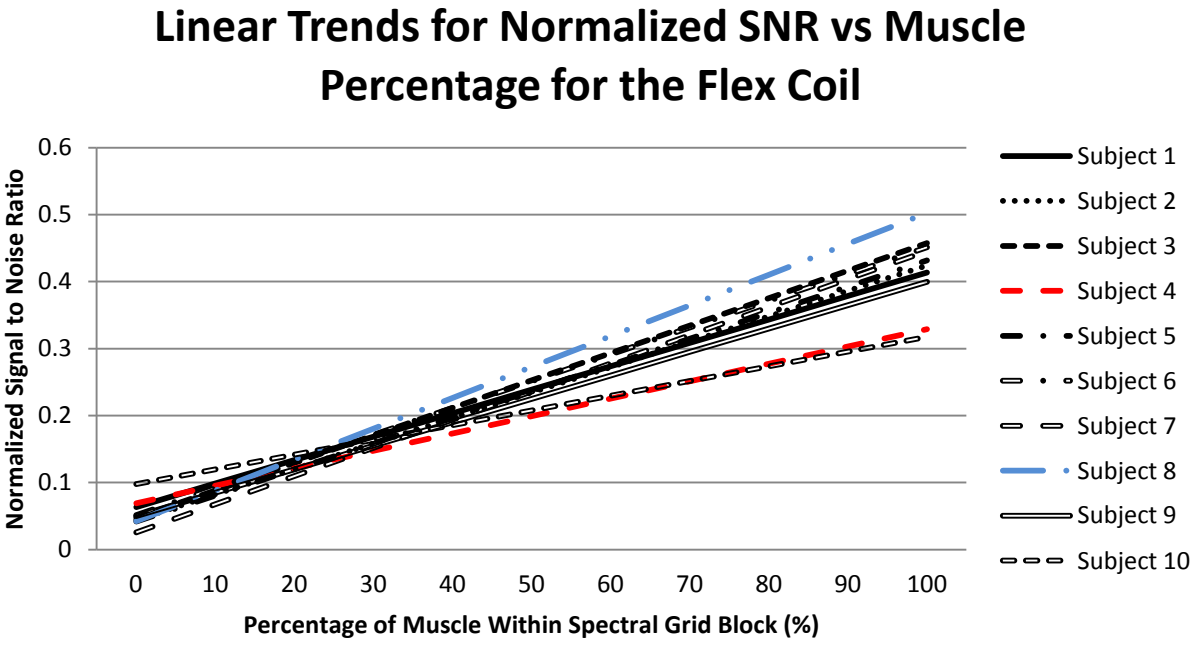

Figure 3.4: The fitted line for each of the subjects' normalized split birdcage coil (top) and flex coil (bottom) data are displayed on the two plots. For the split birdcage coil, with the exception of Subject 8, the trend lines are very closely grouped and follow roughly the same slope. Subject 8's slope is the smallest of the group and Subject 4's slope is the highest of the group. The linear

fits were much worse for the flex coil simply because the flex coil was not as good at acquiring homogeneous signal across the entire FOV like the split birdcage coil. The R^2 values were all less than half of those of the split birdcage coil as seen in table 3.1. Subjects 4 and 8 are again highlighted in the bottom plot, except this time, the smallest slope belongs to subject 10.

the corresponding block, segmentation had to be used. The general signal intensity variation can be seen from both the split birdcage and the flex coil. These variations are due to either a loading effect that a human thigh introduces to the coil or the various distances from the ROI to the center of coil. It is for this reason that a full FOV muscle selection based on voxel signal intensity could not be used. Zooming in to each specific block reduced the variation in signal intensity drastically. However, it did not reduce the variation to zero. It can be seen in the two highlighted blocks of figure 3.2 (the 4^{th} row and the 2^{nd} column of the split birdcage segmentation and the 6^{th} row and the 6^{th} column of the flex coil segmentation) that part of the fat was included in the muscle selection process. Since this was only one block out of the roughly 25 block region taken up by the thigh, it was treated as a small deviation still to be included in producing the eventual trend line generated from the plotted data in figure 3.3.

For the split birdcage coil, because the signal acquisition is uniform across the FOV, the slope of the trend line represents a characteristic of the coil correlating SNR and muscle percentage while the y-intercept represents the noise from the ^{31}P SNR calculation. In an ideal case, the y-intercept should be zero, i.e. a grid block with zero muscle should have zero ^{31}P signal. For the flex coil, the signal intensity, which is proportional to the RF magnetic field, drops off with the distance from the flex coil according to equation 1.3 [43] and so on the far side of the thigh there are blocks of nearly 100 % muscle with almost zero signal intensity. The data

Table 3.1: displays data for the 10 subjects for the linear fit from each subject for the split birdcage coil and the flex coil. It also shows each subject's BMI. The slope and y-intercept values are taken from the normalized SNR plots. The y-intercept is shown as an indicator of the noise present. Theoretically, the y-intercept for each linear fit should be zero, i.e. zero muscle, zero signal or SNR.

Subject	BMI	Split Birdcage Coil			Flex Coil		
		Slope ($x10^{-3}$)	Y-intercept ($x10^{-2}$)	R^2	Slope ($x10^{-3}$)	Y-intercept ($x10^{-2}$)	R^2
1	25.4	8.2	5.94	0.8932	3.5	6.35	0.2934
2	21.8	7.0	2.18	0.7947	3.8	4.43	0.3335
3	20.1	7.4	7.06	0.9003	4.1	4.74	0.3536
4	20.8	8.3	9.30	0.9093	2.6	6.92	0.2027
5	20.6	7.0	6.90	0.8362	3.9	4.16	0.2842
6	30.3	7.2	8.18	0.6899	4.0	5.13	0.3735
7	26.0	8.1	6.53	0.8678	4.2	2.58	0.4777
8	25.4	5.4	8.39	0.5544	4.6	4.24	0.4828
9	27.5	7.0	7.68	0.8176	3.5	4.99	0.2750
10	24.4	6.8	1.95	0.7158	2.2	9.75	0.0988

for the flex coil was also fit with a linear trend line but it is apparent that the flex coil (a surface coil) cannot acquire ^{31}P signal evenly across the FOV. Therefore, the trend line represents less a property of the coil, and more a property of the subject being scanned. For the flex coil, a very small slope for the trend line (subject 10 in figure 4.3, bottom) is indicative of a subject with a greater leg volume with possibly more muscle within that volume. Whereas, a higher trend line slope represents a smaller leg volume so that the flex coil can acquire a higher percentage of muscle blocks. The gradual reduction in signal as distance from the coil increases is reinforced by the visible triangular region that the data falls within, instead of the line that the data for the birdcage falls on.

The body mass index (BMI) of each of the subjects was varied from 20.1 to 30.3, however, from figure 3.4 and table 3.1, there was no significant variation in the data's linear fits

and no discernible relationship between the subjects BMI and the linear fit line. For future studies, a better indicator of the subject should be recorded since BMI does not take into account muscle density or fat content. One option would be to measure the subcutaneous fat thickness under the center of the surface coil and use that as the variable of interest. Table 3.1 shows in conjunction with figure 3.4 that there are two subjects whose best fit slope is on the edges of the group. The two slope values are 0.0083 and 0.0054 from subjects 4 and 8 with BMIs of 20.8 and 24.5 respectively. Table 3.1 shows that subject 4 is actually in a grouping of 3 (subject 1, 4, and 7 with slopes 0.0082, 0.0083, and 0.0081 respectively) with similar slopes whereas subject 8 has a slope that is 23% different than the next smallest slope.

In conclusion, the new split birdcage coil was used to scan 10 subjects in order to obtain a baseline of data for the coil so that future coils could be held to its standard. A segmentation routine was run to compare the ^{31}P signal from PCr to the number of muscle voxels in the same block from which spectral signal was acquired. The data proved to have linear relationships for the split birdcage coil that were fitted with linear regression lines and compared with the flex surface coil. The split birdcage coil showed linear fits that were at least twice as good as the fits from the flex coil. No significant relationship to BMI was found.

CHAPTER 4

AN APPLICATION IN COIL DESIGN

In this chapter, the creation of an electromagnetic 3-axis coil is presented along with simulation results and preliminary experimental results. The design of the coil, which is made to conform to various physical constraints from microscope dimensions to using copper material for the structure, is explained. Simulations were run to show the input current waveforms to the coils in order to obtain a rotating magnetic field in any direction. Preliminary experimental results are displayed for initial tests on micro-beads that are half coated in Nickel(Ni) and magnetized along with some simulation results for the control of helical structures in a 3-D space.

4.1 Introduction

Nano science is a very rapidly developing field of research with many directions and applications. Nano motor refers to a particle on the nano scale that moves either on its own or with the influence of outside control in a medium. It is of interest to a variety of researchers to achieve reliable control over micro and nano scale particles for research in medicine, physics, chemistry, and biology. For the case of micro and nano scale particles within a fluid, such as water or blood, translation of the particle is achieved only with an asymmetric motion. Single cell organisms have been incorporating asymmetric techniques for millions of years in order to move through low Reynolds number media [47, 48]. A macroscopic analogy of a low Reynolds number scenario would be if a person were to swim in a swimming pool filled with molasses at a

rate of 1 cm per minute and expect to make progress. Microorganisms use flagella in order to create the asymmetry. Two ways they can use the flagella are to wave it like a flag [49], or to spin it like a corkscrew [47, 48, 50, 51]. The fabrication and growth of helical tails on a 'head' is popular. Some examples include self-scrolling flagella [48, 51] and the shadow-growth method, also known as glancing angle deposition [50]. Both of these methods are used to create helical structures. This type of nano particle, if grown with magnetic material, can be controlled by a magnetic field (e.g. produced by a pair of Helmholtz coils). It is possible to create a rotating magnetic field so that a nano helix that continuously realigns with the magnetic field, in fact drills through the low Reynolds number medium. In the past, research groups have been able to control magnetic micro or nano sized particles using expensive commercially built coils [48, 51] and particles that have either a magnetic tip [48, 51, 52] or coating along one side [50]. These groups have been able to show the feasibility of maneuvering structures through micro-channel paths and using them to push objects.

Presented in the following sections are the details for construction of the 3-axis coil along with some preliminary experimental results of rotations of micro-beads and simulations that show how magnetic field control in any direction is possible.

4.2 Design and Experimental Setup

The design of the 3-axis electro magnet revolved around being able to control magnetic particles in each of the three Cartesian coordinate planes, xy, yz, and zx while conforming to the constraints of the microscope to be used and the overall size of the coil. The apparatus, called the 3-axis coil, was made of three pairs of Helmholtz coils. A Helmholtz coil uses two separate windings of wire running a current through each with the same magnitude and direction.

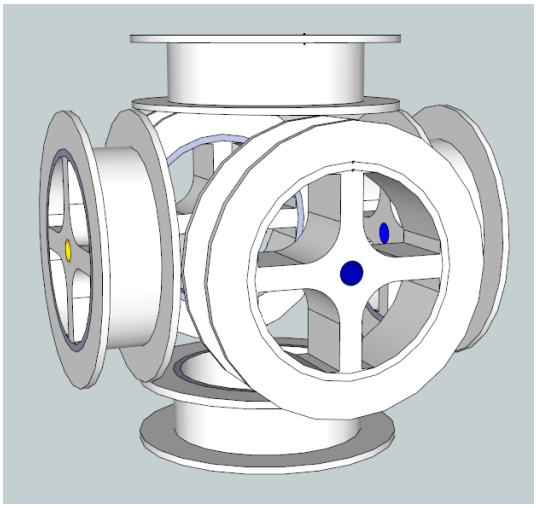

Figure 4.1: Schematic of the 3-axis coil with proposed spool supports to center a translation stage on which micro-beads were viewed and on which nano motors could be viewed. Designed with Google SketchUp software.

Refer to Chapter 1, figure 1.2 for the diagram. The spacing of the coils for a maximized uniform field between the pair of coils is such that the distance between the coils is equal to the radius of the coils. Each pair of coils in our experiment uses a separation larger than the radius of the coils primarily because of the restraints of the microscope and the other coil pairs in close proximity. The coils needed to have an inner diameter large enough for the objective lens of the microscope to fit through for viewing of the particles. The inner diameter was made to be 5.1 cm. The other constraint, coils in close proximity to each other, dictated that to have symmetry, the outer diameter of each spool would have to be 7.5 cm and each spool would be 2.0 cm thick. Therefore, given a wall thickness of 0.2 cm, the area for coil windings would be 1.6 cm by 1.0 cm. Refer to figure 4.2. The magnetic field at a point with distance of x from the coil along its axis is found from the equation,

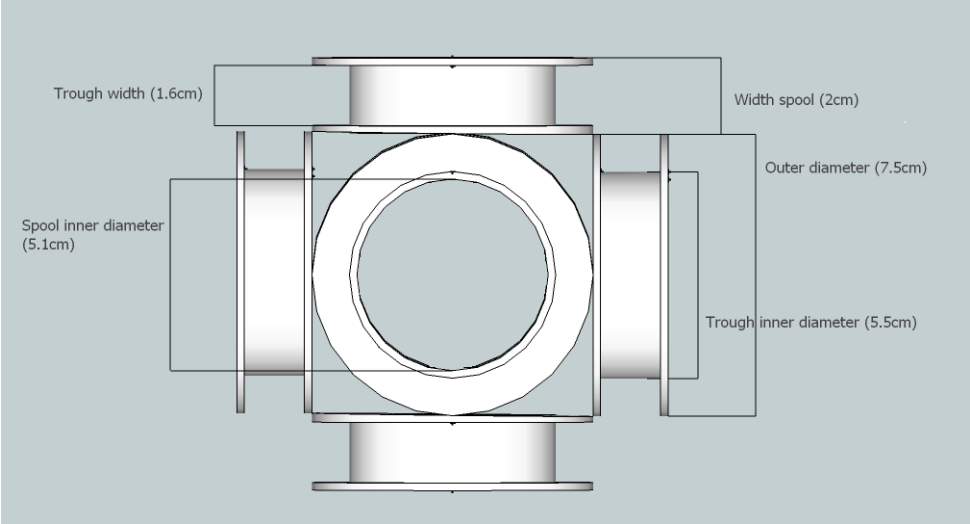

Figure 4.2: Schematic of the 3-axis coil from the top down. The top and bottom spools are left open so that the objective lens of a microscope can be maneuvered to the center of the coil.

$$B = \frac{\mu_0 n I R^2}{2(R^2+x^2)^{3/2}} \tag{4.1}$$

where B is the magnetic field, μ_0 is the permeability of free space, n is the number of turns, I is the current through each coil, and R is the radius of the coils. To find the field at the center of two coils and in close proximity of the center, a multiplicative factor of two was used for a centered point between the coils in the Helmholtz coil pair equation from Chapter 1, equation 1.4, to simplify the two fractional components into one. For this coil spacing, a current of 1 A sent through the 90 turns produces a homogeneous magnetic field of 0.70 mT. The direct relationship between the magnetic field and the current dictate that if the current were increased, the magnetic field would also linearly increase.

Six single wound coils were placed as if on the sides of a cube to form the 3-axis coil. These spools for each single wound coil, were made from copper because of its very low

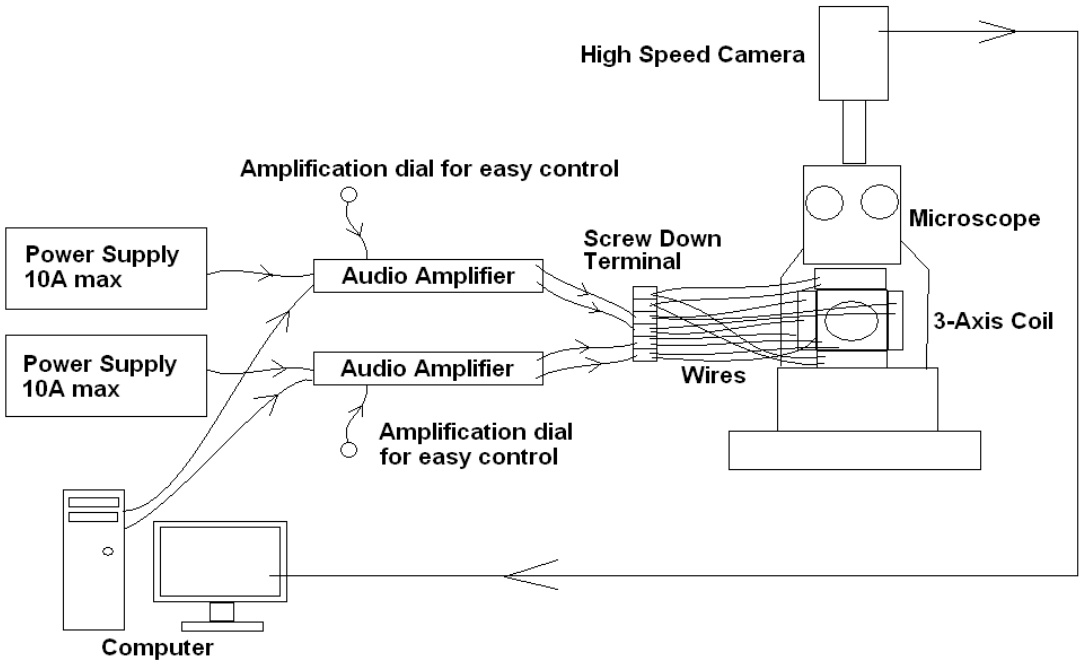

Figure 4.3: Schematic displaying the experimental setup, including the computer, amplifiers, power supplies, microscope, and 3-axis coil.

magnetic susceptibility of -0.92. Each spool was wound with copper gauge 16 magnet wire with a durable coating on the outside. Ninety turns were uniformly hand wound on each spool along with an input lead and an output lead that were left to be connected later.

The control of the 3-axis coil came from a computer, audio amplifiers, power supplies, an oscilloscope, and a current probe, that, through LabView, produced an amplified AC signal that was input to the coil. LabView communicated with the two channel audio port of the computer to send the signal to the amplifiers. The amplifiers, powered by the laboratory grade power supplies, were slowly turned on until the connected current probes detected a current to the coil as seen on the oscilloscope. Figure 3 shows the experimental setup.

The particles used in the experiment were 9.9 μm diameter polystyrene micro-beads coated with 100 nm Ni on one hemisphere. These beads were magnetized along the polar axis in a uniform magnetic field of 45 mT. The beads were then put into a glass capillary tube containing de-ionized water which has a viscosity of 1.002×10^{-3} Ns/m^2.

4.3 Simulation and Theory

The coil developed to create a rotating magnetic field to drive micro and nano sized particles consisted of three pairs of Helmholtz coils each directed on one of the three Cartesian axes, centered on a ROI about 1 cm x 1 cm x 1 cm. One of the three pairs was used with a constant direct current (DC) power while the other two were used with an alternating current (AC) power that had a 90 degree phase shift from each other. This 90 degree shift with a sinusoidal AC input wave created a rotating magnetic field perpendicular to the DC aligning field. The use of the coil in this manner allowed for use in six directions, +x, -x, +y, -y, +z, and –z. Table 1 shows the strength of the field generated with varying current values through the coils.

When multiple magnetic fields are concerned, the resultant magnetic field is simply the vector sum of each individual field. Therefore, it is possible to create the same effect of having an aligning magnetic field plus a perpendicular rotating magnetic field with three sets of coils oriented along the three Cartesian axes. By treating the resultant magnetic field as a vector originating from the origin, the motion of the tip of the vector can be projected to the x-, y-, and z-axes.

The particle will only have motion if the magnetic field from the coils produces a driving torque

$$T_d = m \times B \tag{4.2}$$

on the particle strong enough to overcome the viscous forces of the medium. In equation 4.2, T_d, m, and B are vector quantities for the driving torque, magnetization of the micro-bead, and magnetic field generated by the coils respectively. For a particle in a low Reynolds number medium (water on this scale is a low Reynolds number media) close to the surface of the container, the viscous torque that needs to be overcome is given by

$$T_v = \frac{8\pi\mu_0 a^3 \Omega}{1-\frac{1}{8}(a/\delta)^3} \tag{4.3}$$

where T_v is the viscous torque, a is the radius of the microbead, Ω is the angular velocity, and δ is the distance between the micro-bead and the boundary [53].

4.4 Results

4.4.1 Preliminary Experimental Results

The preliminary results for the micro-bead include observations of spinning and rolling along the boundary of the capillary tube at various frequencies, ω. Table 4.1 shows the speeds that the micro-beads roll across the microscope's FOV related to various driving frequencies. The speed was measured by observing a recorded video of the motion and dividing the distance traveled by the time it took to get there. Visual inspection is an important part of recording results for these particles because of their size. It can be seen in the series displayed in figure 4.6 that the 9.9 μm diameter micro-bead is rotating in a counterclockwise direction corresponding to the xy-plane. Figure 4.7 shows the micro-bead in the y-z plane rolling up the FOV followed by a large piece of debris. Notice how the smaller unmagnetized particles remain stationary while the bead and the debris roll.

Table 4.1: Shows three cases for the two planes in which rolling occurs, 1 Hz, 2 Hz, and 3 Hz for the xz-plane and the yz-plane. The signal transmitted from the computer was observed to be different than the desired frequency by 11%.

Plane of Rotation	Driving Frequency (Hz)	Observed Frequency (Hz)	Speed (μm/s)
xz	1	1.11	2.53
xz	2	2.22	4.91
xz	3	3.33	7.49
yz	1	1.11	2.27
yz	2	2.22	5.48
yz	3	3.33	8.27

4.4.2 Mathematical Derivation of Control in any Direction

Starting with the equation of a circle centered on the origin in the xy-plane, rotation matrices about the +x-axis and the +z-axis were applied to give the x-, y-, and z-components of a circular motion in some direction corresponding to polar coordinate variables θ and φ over time. Figure 4.6 shows the polar notation used. The aligning component was added afterwards to produce an offset from the origin that corresponds to the aligning magnetic field. By combining these two components, the rotating field and the aligning field, the result is a vector that traces out a cone whose tip is centered on the origin.

Equations 4.4 through 4.7 show the calculation the rotating portion of the equivalent magnetic field with respect to the three Cartesian directions in terms of time, frequency of rotation, magnitude of the rotating magnetic field, and polar angles θ and φ. This series starts with a circular rotating field in the xy-plane. Equation 4.4 shows that the initial forms of x, y, and z give the equation of a circle in the xy-plane with amplitude, A, frequency, ω, and time, t.

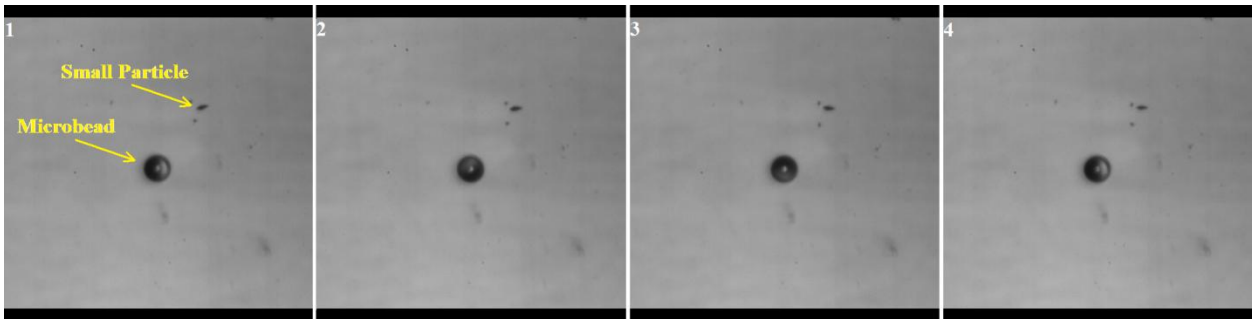

Figure 4.4: A series of four images taken from a movie of the rotating micro-bead. The rotation is apparent from the bright side of the bead. The brighter effect is caused by light reflecting off of half of the bead from the coating and not the other half. Also, the small particle above and to the right of the micro-bead shows no rotation for the reason of not being magnetized like the bead.

$$\begin{bmatrix} x \\ y \\ z \end{bmatrix} = \begin{bmatrix} A\sin\omega t \\ A\cos\omega t \\ 0 \end{bmatrix} \tag{4.4}$$

These equations are then rotated with the rotation matrices for a rotation about the +x-axis of φ degrees followed by a rotation about the +z-axis of θ degrees. X, Y, and Z represent the rotated circle in terms of φ, θ, and the original unrotated x, y, and z.

$$\begin{bmatrix} X \\ Y \\ Z \end{bmatrix} = \begin{bmatrix} \cos\theta & -\sin\theta & 0 \\ \sin\theta & \cos\theta & 0 \\ 0 & 0 & 1 \end{bmatrix} \begin{bmatrix} 1 & 0 & 0 \\ 0 & \cos\varphi & -\sin\varphi \\ 0 & \sin\varphi & \cos\varphi \end{bmatrix} \begin{bmatrix} x \\ y \\ z \end{bmatrix} \tag{4.5}$$

Plugging in the equations for the circle from equation 4.4, and carrying out the matrix multiplication, equation 4.7 is the result.

$$\begin{bmatrix} X \\ Y \\ Z \end{bmatrix} = \begin{bmatrix} \cos\theta & -\sin\theta & 0 \\ \sin\theta & \cos\theta & 0 \\ 0 & 0 & 1 \end{bmatrix} \begin{bmatrix} 1 & 0 & 0 \\ 0 & \cos\varphi & -\sin\varphi \\ 0 & \sin\varphi & \cos\varphi \end{bmatrix} \begin{bmatrix} A\sin\omega t \\ A\cos\omega t \\ 0 \end{bmatrix} \tag{4.6}$$

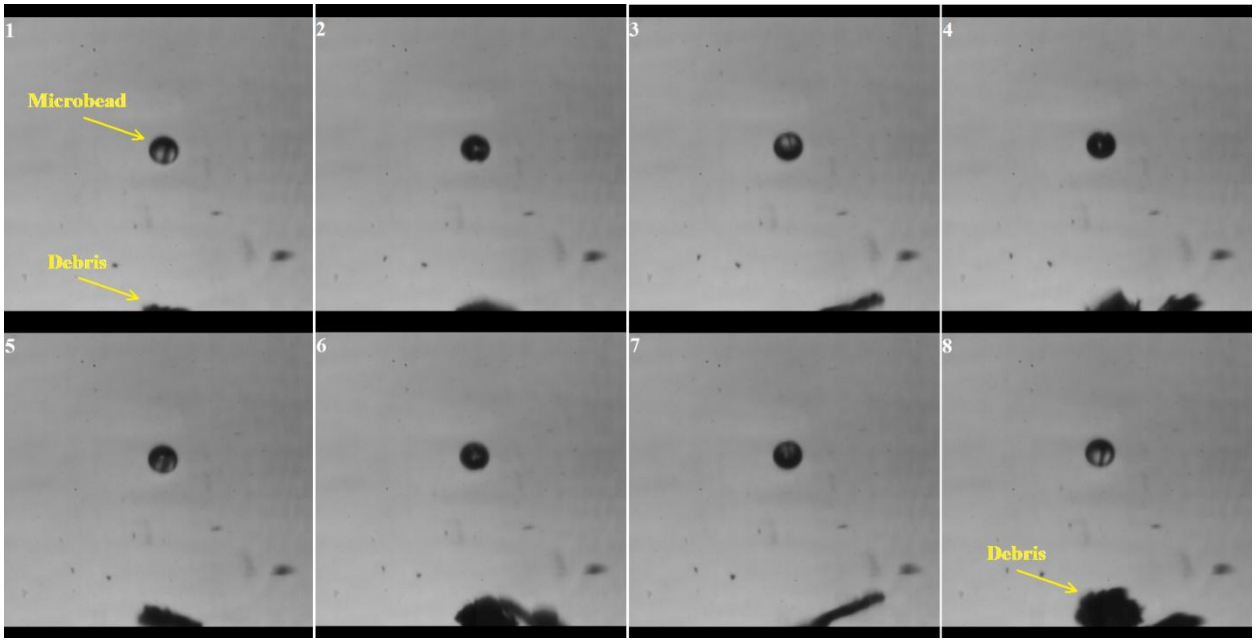

Figure 4.5: Shown in this figure is a micro-bead rolling in the yz-plane (from the bottom to the top) followed by a large piece of debris that is rolling in the same direction. The bead is unaffected by the presence of the debris. The micro-bead has some sort of cleft side that can be seen in frames 1, 2, 4, and 8 clearly. This is due to a slightly uneven coating of Ni.

$$\begin{bmatrix} X \\ Y \\ Z \end{bmatrix} = \begin{bmatrix} A\cos\theta\sin\omega t - A\cos\varphi\sin\theta\cos\omega t \\ A\sin\theta\sin\omega t + A\cos\varphi\cos\theta\cos\omega t \\ A\sin\varphi\cos\omega t \end{bmatrix} \tag{4.7}$$

Equation 4.7 gives an expression for *X*, *Y*, and *Z*, the rotated circle. Drawing a vector from the origin and tracing the rotated circle represents the rotating magnetic field. X, Y, and Z are the waveforms in the x-, y-, and z-directions necessary to generate the field.

Equations 4.8 through 4.10 show the calculation of the aligning component of the equivalent magnetic field in terms of time, rotating magnetic field magnitude, polar angles θ and φ, and proportionality value between the aligning field and the rotating field. The series starts

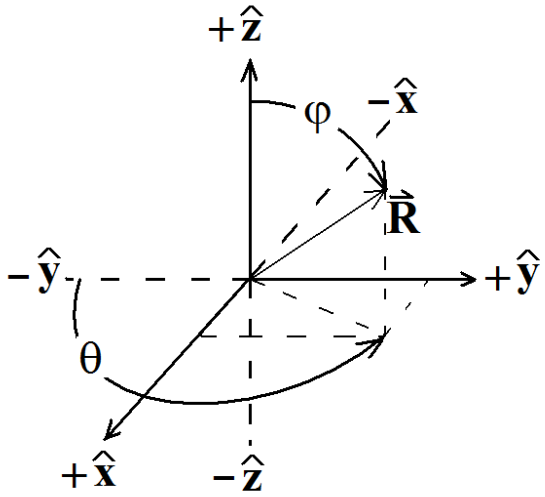

Figure 4.6: Polar coordinate system used for derivations and simulation of Cartesian components of resultant magnetic field.

with a vector in the z-direction. The variables, r_x, r_y, and r_z represent the unrotated vector in the z-direction which is a multiple, n, of the rotating magnetic field magnitude.

$$\begin{bmatrix} r_x \\ r_y \\ r_z \end{bmatrix} = \begin{bmatrix} 0 \\ 0 \\ nA \end{bmatrix} \tag{4.8}$$

Similar to the rotations of the rotating magnetic field, the vector for the aligning component of the field is rotated first about the +x-axis by φ degrees followed by a rotation about the +z-axis of θ degrees. In equations 4.9 and 10, R_x, R_y, and R_z represent the rotated form of the original vector defined by r_x, r_y, and r_z.

$$\begin{bmatrix} R_x \\ R_y \\ R_z \end{bmatrix} = \begin{bmatrix} \cos\theta & -\sin\theta & 0 \\ \sin\theta & \cos\theta & 0 \\ 0 & 0 & 1 \end{bmatrix} \begin{bmatrix} 1 & 0 & 0 \\ 0 & \cos\varphi & -\sin\varphi \\ 0 & \sin\varphi & \cos\varphi \end{bmatrix} \begin{bmatrix} 0 \\ 0 \\ nA \end{bmatrix} \tag{4.9}$$

$$\begin{bmatrix} R_x \\ R_y \\ R_z \end{bmatrix} = \begin{bmatrix} nA\sin\theta\sin\varphi \\ -nA\cos\theta\sin\varphi \\ nA\cos\varphi \end{bmatrix} \tag{4.10}$$

Combining the components for the rotating magnetic field, equation 4.7, and the aligning field, equation 4.10, yields the x-, y-, and z-projections for the Cartesian directions.

$$X = A\cos\theta\sin\omega t - A\cos\varphi\sin\theta\cos\omega t + nA\sin\theta\sin\varphi \tag{4.11}$$

$$Y = A\sin\theta\sin\omega t + A\cos\varphi\cos\theta\cos\omega t - nA\cos\theta\sin\varphi \tag{4.12}$$

$$Z = A\sin\varphi\cos\omega t + nA\cos\varphi \tag{4.13}$$

4.5 Discussion

The design of this experiment was to show feasibility to control micro and nano scale particles and observe it from a microscope. The coil, the particles, and the software were all developed or constructed in the lab. The electromagnetic 3-axis coil made up of Helmholtz pairs was able to control magnetic micro-beads which have a higher viscous torque than a nano helix would have and so the possibility for driving helical structures, not just with commercial implementation [50-52] is very real.

The setup of the experiment was made to fit the confines of a microscope platform with enough extra space to be able to focus the microscope. Ideally, the Helmholtz coils should have been placed closer together to achieve the optimum homogeneity in the center of the coil system. However, the particles are small enough that they were not observed to be affected by the less than ideal field homogeneity. For all intents and purposes, the field was approximately uniform for the range that the particle could move. The measurements of speed and rotation frequency from table 4.1 were found from videos taken of the micro-beads. It turned out that the measured frequency was greater than the desired frequency by 11%. This difference, since it wasn't a reduction in frequency, was probably attributed to a flaw in the computer program for the coil control. LabView (National Instruments, Austin, TX) was used to generate the desired

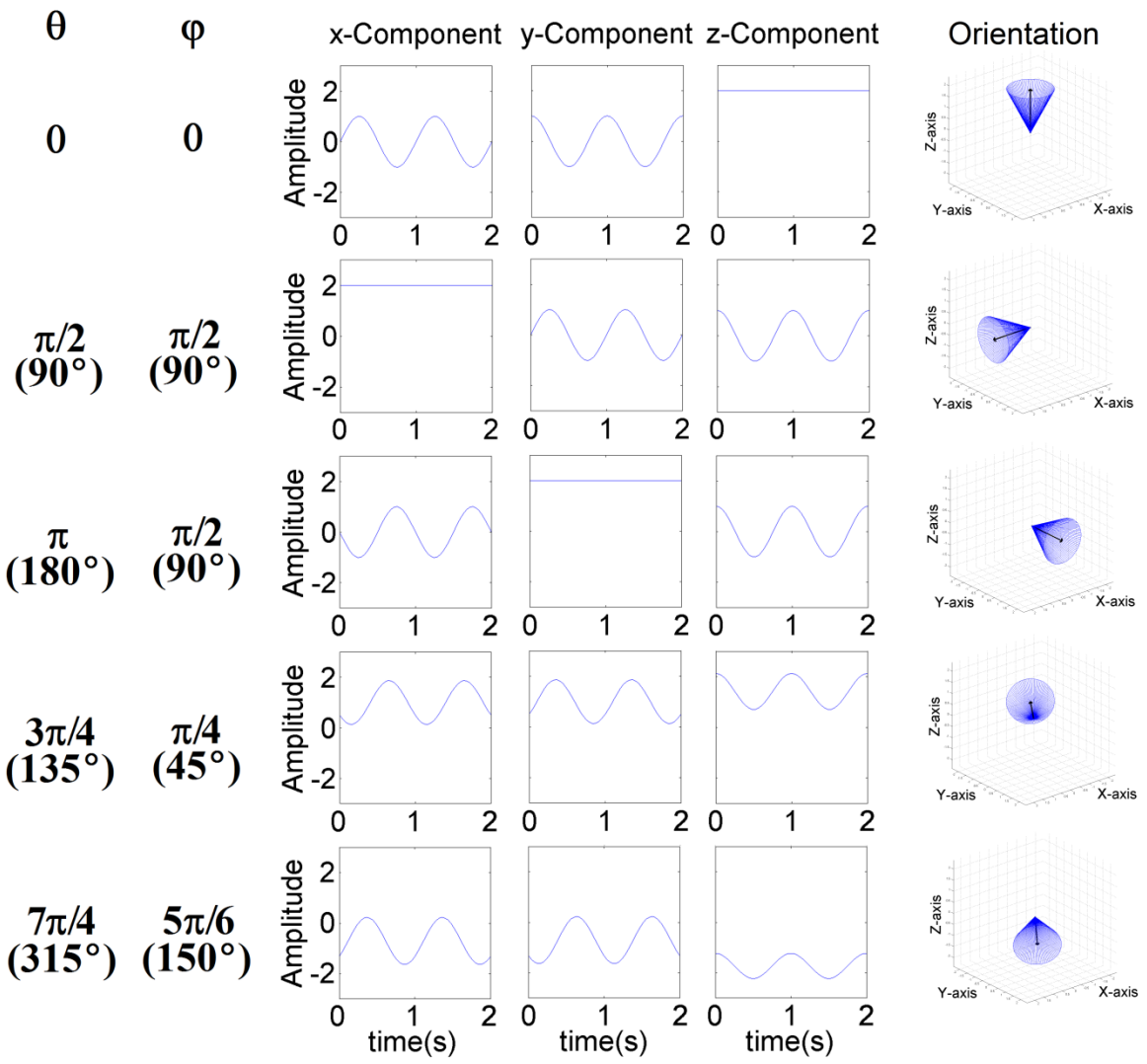

Figure 4.7: This depicts the implementation of equations 4.11, 12, and 13 to produce x-, y-, and z-components of the current to input to the coils in order to produce a rotating magnetic field in the direction given by the polar coordinates indicated. The frequency is 1 Hz and the ratio of aligning magnetic field to rotating magnetic field is 2. The first three series represent rotations about the +z-, +x-, and +y axes respectively. The 4^{th} and 5^{th} series are not as straight forward. The 4^{th} series represents a rotation about a vector pointing in the quadrant bound by the +x-, +y-, and +z-axes while the 5^{th} series represents a rotation about a vector pointing in the quadrant bound by the –x-, –y-, and –z-axes.

sinusoidal wave with an offset, if necessary, to send to the audio port of the computer. This was an ideal port because stereo output has two channels. Output from the two-channel audio port was amplified and then sent to the coil. If there had been a reduction in frequency, it might have been the amplifiers that were slowing it down. However, it's more likely that the problem was in the program generating a signal for the audio ports because of the constant value that they were different.

The speed measurements from table 4.1 were slightly different from the xz-plane to the yz-plane. For 1 Hz, 2 Hz, and 3 Hz, the xy-plane speed was smaller by 10%, greater by 10%, and greater by 10% than that of yz-plane, respectively. Since one is not consistently smaller or greater than the other, it was assumed that the recorded values were within normal error readings. Possible sources of error include difference of driving current in the coil, very slight fluid currents in the medium in which the particles are suspended, interaction with smaller particles close by, or irregularities on the surface of the boundary or the micro-bead.

The simulation results were meant to show a method for using the computer to control the coils so that a rotating magnetic field could be generated in any direction and therefore, translation could be achieved in any direction. Figure 4.7 shows what looks like a series of sinusoidal waves or constant values for the x-, y-, and z-projections of the magnetic field for any given instant. The orientation plots on the right side of the figure show the resultant magnetic field cone produced with the addition of the rotating magnetic field and the aligning magnetic field. One variable that remained constant through the simulations was the factor for the aligning magnetic field to the rotating magnetic field. This was left at a value of 2, meaning the amplitude of the aligning magnetic field was twice that of the rotating magnetic field. The higher the ratio

is, the sharper the cone looks. This allows the rotating magnetic field to not overpower the aligning field so that the particles nano particles will stay on track.

In conclusion, the half-coated, magnetized, 9.9 μm beads proved to be easily manipulated with the homemade 3-axis coil. Spinning was observed in the xy-plane and rolling was observed in the yz- and xz-planes at small frequencies 1, 2, and 3 Hz. The coils were successfully driven with LabView and controlled through the computer's audio output with two phase shifted currents. Simulations were also run to show the steps toward creating a rotating magnetic field in any direction with the same 3-axis coil.

CHAPTER 5

CONCLUSIONS AND FUTURE WORK

5.1 Split Birdcage Coil

The split birdcage coil is not the first version of a dual-tuned birdcage coil that was built for the purpose of acquiring multinuclear (e.g. ^{31}P) spectroscopic data. It is however, a new coil that takes into consideration a very important aspect of the building process that is sometimes glossed over, ease of construction. Several variations of the dual-tuned birdcage coil were attempted (e.g. , 4-ring LP-LP, split LP-LP, split LP-HP) and it was found that the final design (split LP-HP) best fit the needs of the experiment, in addition to having a large multinuclear sampling volume and being able to scale the coil to the anatomy of the human thigh like other variations. The idea for the split birdcage coil was inspired in an effort to reduce the number of iterations for tuning and matching. It also helped to reduce the time required to tweak the tuning between scans for subjects that introduced different loading effects to the coil. For example, switching from a phantom bottle to a human subject produced a large difference in loading in and around the coil.

It was found that the easy construction and use of the new split birdcage coil outweighed its slight reduction of coil sensitivity and field homogeneity for ^{1}H excitation as seen in figure 2.2 in its comparison with the 4-ring birdcage coil. Its acquisition of ^{31}P outperformed the commercially available and previously used flex surface coil in terms of uniform ^{31}P signal across the entire FOV that was scanned.

The experiment's results showed that localizing ^{31}P signal to a cubic voxel approximately 2 cm a side is possible, as well as important, with the FID CSI sequence. However, because the signal from ^{31}P is weak as compared to ^{1}H, extracting signal from a slightly larger region corresponding to a muscle or muscle group would be more useful. This would include extending the acquisition in the z-direction to account for muscles sometimes being long and thin. By acquiring ^{31}P signal from PCr, exercise regimens targeting muscle groups deep in the tissue could be evaluated. The next step for the split birdcage coil might be to either use it for time sensitive studies where relaxation coefficients are being measured or build another one tailored to scan another part of the body such as the human head instead of the human thigh. Multinuclear (^{31}P) analysis of the human head is important for various studies like the classification and diagnosis of cerebral tumors [20]. A coil of this nature would take into account the considerations of the subject in the scanner, such as comfort, room to breathe, and efficiency so that fewer averages would need to be acquired in turn reducing scan time.

5.2 Verification of the Split Birdcage Coil by a Ten-Subject Study

The goal of the study was to acquire a baseline of data with the new split birdcage coil that could be used in the future as a standard to hold the coil's performance to. To accomplish this, the SNR of every grid block's PCr peak from each subject was correlated with the corresponding percentage of muscle from the same grid block as seen in the anatomical image. A muscle/fat segmentation method, developed by the UGA Department of Kinesiology, was altered to be useful on an image map that had some signal intensity variation across the FOV. The FOV was divided into grid blocks corresponding to the FID CSI grid and then it was used to isolate the muscle in each grid block. This method of comparing the PCr SNR to the percentage of

muscle is in fact a very useful method of measuring the coil's performance because it relates both parts of the coil, the ^{1}H structures and the ^{31}P structure, in a two-in-one fashion by using a linear trend line for comparison between the ten subjects.

It was found that the split birdcage coil, because of its uniform ^{31}P field across the FOV, had a linear relationship between PCr SNR and percentage of muscle. The flex coil, which was also tested in this study did not prove to have uniform PCr SNR coverage across the FOV because of its nature as a surface coil. This produced data that when fit with a linear trend line, produced R^2 values that were less than half of those of the split birdcage plots. For the flex coil, this method of data analysis provided more characteristics of the loading for the coil instead of characteristics of the coil itself. For example, a leg, small in volume would have a larger slope from the trend line as well as a larger R^2 value than a leg of larger volume because the flex coil would be able to measure more of the leg. However, a leg that is large in volume means the flex coil would be able to only acquire signal from a region close to the coil. This would create more grid blocks with muscle yet no PCr peak, a smaller slope, and in turn, a smaller R^2 value than a leg with smaller volume.

The key to using volume coils over surface coils is the need to look at more than one area in the sample or the need to look deep within the sample. The future of this work would go hand in hand with the future of the split birdcage coil itself. Future coils and future uses of the split birdcage coil can be held to the standard obtained in this baseline study.

5.3 Application for Micro Sized Particle Locomotion

The three-axis coil that was built for this experiment uses the same electromagnetic theory of Helmholtz coil pairs that modern MRI uses to generate images of the human body. The

rotating magnetic field, though operating at a very low frequency (a few Hertz), uses the same ideas that a RF birdcage coil uses where as the birdcage works at a much higher frequency (tens or hundreds of mega-Hertz). Both coils use a sinusoidal wave pattern to generate the rotation. The birdcage coil, with quadrature excitation, uses two sinusoidal inputs with a phase shift of 90 degrees to create a circularly polarized magnetic field to achieve resonance at the desired frequency. The three-axis coil uses two sinusoidal waves with a phase shift of 90 degrees, to control the precise rotational field of two pairs of Helmholtz coils. The coil was shown effective with the manipulation of a 9.9 μm micro-bead.

It was found that a rotating magnetic field in any direction with only three pairs of Helmholtz coils could easily be created by rotating a circle offset from the origin by polar angles φ and θ. The B-field projections onto the three Cartesian axes then translate into alternating currents to input to the coil.

The usefulness of this project lies in its function of making an eventual experiment involving helical nano motors easier to carry out. For this particular type of experiment, the laboratory conditions and setup play a large role in constraining the experiment. However, by building a custom coil that fits with the available microscope and creating a method of control based in the computer to maneuver nano structures in any direction, some of the experimental constraints are removed. Whether the experiment is navigating micro channels [52], interacting with another particle (perhaps a drug to be delivered) [51], or if it is interacting with a viscosity barrier (such as water to oil), the work presented here will help facilitate the acquisition of the goal at hand.

BIBLIOGRAPHY

[1] P. Mansfield and A. A. Maudsley, "Medical imaging by NMR," *Br J Radiol,* vol. 50, pp. 188-94, Mar 1977.

[2] P. Mansfield, I. L. Pykett, and P. G. Morris, "Human whole body line-scan imaging by NMR," *Br J Radiol,* vol. 51, pp. 921-2, Nov 1978.

[3] P. C. Lauterbur, "Progress in n.m.r. zeugmatography imaging," *Philos Trans R Soc Lond B Biol Sci,* vol. 289, pp. 483-7, Jun 25 1980.

[4] F. Bloch, "The Principle of Nuclear Induction," *Science,* vol. 118, pp. 425-30, Oct 16 1953.

[5] E. M. Purcell, "Nuclear Magnetism in Relation to Problems of the Liquid and Solid States," *Science,* vol. 107, pp. 433-40, Apr 30 1948.

[6] Rabi, II, "The Atomic Nucleus, A New World to Conquer," *Science,* vol. 108, pp. 673-5, Dec 17 1948.

[7] K. J. Cureton, P. D. Tomporowski, A. Singhal, J. D. Pasley, K. A. Bigelman, K. Lambourne, J. L. Trilk, K. K. McCully, M. J. Arnaud, and Q. Zhao, "Dietary quercetin supplementation is not ergogenic in untrained men," *J Appl Physiol,* vol. 107, pp. 1095-104, Oct 2009.

[8] S. C. Forbes, A. T. Paganini, J. M. Slade, T. F. Towse, and R. A. Meyer, "Phosphocreatine recovery kinetics following low- and high-intensity exercise in human

triceps surae and rat posterior hindlimb muscles," *Am J Physiol Regul Integr Comp Physiol,* vol. 296, pp. R161-70, Jan 2009.

[9] S. C. Forbes, J. M. Slade, R. M. Francis, and R. A. Meyer, "Comparison of oxidative capacity among leg muscles in humans using gated 31P 2-D chemical shift imaging," *NMR Biomed,* vol. 22, pp. 1063-71, Dec 2009.

[10] G. Goldstein, K. Panchalingam, R. J. McClure, J. A. Stanley, V. D. Calhoun, G. D. Pearlson, and J. W. Pettegrew, "Molecular neurodevelopment: An in vivo P-31-H-1 MRSI study," *J Int Neuropsychol Soc,* vol. 15, pp. 671-683, Sep 2009.

[11] O. Gonen, J. Hu, J. Murphy-Boesch, R. Stoyanova, and T. R. Brown, "Dual interleaved 1H and proton-decoupled-31P in vivo chemical shift imaging of human brain," *Magn Reson Med,* vol. 32, pp. 104-9, Jul 1994.

[12] O. Gonen, J. Murphy-Boesch, R. Srinivasan, J. Hu, H. Jiang, R. Stoyanova, and T. R. Brown, "Simultaneous and interleaved multinuclear chemical-shift imaging, a method for concurrent, localized spectroscopy," *J Magn Reson B,* vol. 104, pp. 26-33, May 1994.

[13] R. L. Greenman and H. A. Smithline, "The Feasibility of Measuring Phosphocreatine Recovery Kinetics in Muscle Using a Single-shot (31)P RARE MRI Sequence," *Acad Radiol,* Apr 30 2011.

[14] G. J. Kemp and G. K. Radda, "Quantitative interpretation of bioenergetic data from 31P and 1H magnetic resonance spectroscopic studies of skeletal muscle: an analytical review," *Magn Reson Q,* vol. 10, pp. 43-63, Mar 1994.

[15] K. K. McCully, T. K. Mulcahy, T. E. Ryan, and Q. Zhao, "Skeletal muscle metabolism in individuals with spinal cord injury," *J Appl Physiol,* vol. 111, pp. 143-8, Jul 2011.

[16] K. K. McCully, S. Smith, S. Rajaei, J. S. Leigh, Jr., and B. H. Natelson, "Muscle metabolism with blood flow restriction in chronic fatigue syndrome," *J Appl Physiol,* vol. 96, pp. 871-8, Mar 2004.

[17] K. K. McCully, T. N. Turner, J. Langley, and Q. Zhao, "The reproducibility of measurements of intramuscular magnesium concentrations and muscle oxidative capacity using 31P MRS," *Dyn Med,* vol. 8, p. 5, 2009.

[18] J. L. Olive, G. A. Dudley, and K. K. McCully, "Vascular remodeling after spinal cord injury," *Med Sci Sports Exerc,* vol. 35, pp. 901-7, Jun 2003.

[19] F. Podo, "Tumour phospholipid metabolism," *NMR Biomed,* vol. 12, pp. 413-39, Nov 1999.

[20] J. Solivera, S. Cerdan, J. M. Pascual, L. Barrios, and J. M. Roda, "Assessment of 31P-NMR analysis of phospholipid profiles for potential differential diagnosis of human cerebral tumors," *NMR Biomed,* vol. 22, pp. 663-74, Jul 2009.

[21] Y. Duan, B. S. Peterson, F. Liu, T. R. Brown, T. S. Ibrahim, and A. Kangarlu, "Computational and experimental optimization of a double-tuned (1)H/(31)P four-ring birdcage head coil for MRS at 3T," *J Magn Reson Imaging,* vol. 29, pp. 13-22, Jan 2009.

[22] R. L. Greenman and R. Rakow-Penner, "Evaluation of the RF field uniformity of a double-tuned 31P/1H birdcage RF coil for spin-echo MRI/MRS of the diabetic foot," *J Magn Reson Imaging,* vol. 22, pp. 427-32, Sep 2005.

[23] T. Lanz, M. von Kienlin, W. Behr, and A. Haase, "Double-tuned four-ring birdcage resonators for in vivo 31P-nuclear magnetic resonance spectroscopy at 11.75 T," *MAGMA,* vol. 5, pp. 243-6, Sep 1997.

[24] G. B. Matson, P. Vermathen, and T. C. Hill, "A practical double-tuned 1H/31P quadrature birdcage headcoil optimized for 31P operation," *Magn Reson Med,* vol. 42, pp. 173-82, Jul 1999.

[25] J. Murphy-Boesch, R. Srinivasan, L. Carvajal, and T. R. Brown, "Two configurations of the four-ring birdcage coil for 1H imaging and 1H-decoupled 31P spectroscopy of the human head," *J Magn Reson B,* vol. 103, pp. 103-14, Feb 1994.

[26] J. R. Fitzsimmons, B. L. Beck, and H. R. Brooker, "Double resonant quadrature birdcage," *Magn Reson Med,* vol. 30, pp. 107-14, Jul 1993.

[27] A. M. Hudson, W. Kockenberger, and R. W. Bowtell, "Dual resonant birdcage coils for 1H detected 13C microscopic imaging at 11.7 T," *Magn Reson Mater Phy,* vol. 10, pp. 61-8, Jun 2000.

[28] P. M. Joseph and D. Lu, "A technique for double resonant operation of birdcage imaging coils," *IEEE Trans Med Imaging,* vol. 8, pp. 286-94, 1989.

[29] B. Tomanek, V. Volotovskyy, M. L. H. Gruwel, E. McKenzie, and S. B. King, "Double-frequency birdcage volume coils for 4.7T and 7T," *Concepts Magn Reson Part B Magn Reson Eng,* vol. 26B, pp. 16-22, Aug 2005.

[30] C. E. Hayes, "The development of the birdcage resonator: a historical perspective," *NMR Biomed,* vol. 22, pp. 908-918, Nov 2009.

[31] A. M. Hudson, W. Kockenberger, and R. W. Bowtell, "Open access birdcage coils for microscopic imaging of plants at 11.7 T," *Magn Reson Mater Phy,* vol. 10, pp. 69-74, Jun 2000.

[32] M. C. Leifer, "Resonant modes of the birdcage coil," *J Magn Reson,* vol. 124, pp. 51-60, Jan 1997.

[33] M. Lupu, J. L. Dimicoli, A. Volk, and J. Mispelter, "An efficient design for birdcage probes dedicated to small-animal imaging experiments," *Magn Reson Mater Phy*, vol. 17, pp. 363-71, Dec 2004.

[34] A. R. Rath, "Design and Performance of a Double-Tuned Bird-Cage Coil," *J Magn Reson*, vol. 86, pp. 488-495, Feb 15 1990.

[35] J. Chen, Z. Feng, and J. M. Jin, "Numerical simulation of SAR and B1-field inhomogeneity of shielded RF coils loaded with the human head," *IEEE Trans Biomed Eng*, vol. 45, pp. 650-9, May 1998.

[36] C. M. Collins, S. Li, and M. B. Smith, "SAR and B1 field distributions in a heterogeneous human head model within a birdcage coil. Specific energy absorption rate," *Magn Reson Med*, vol. 40, pp. 847-56, Dec 1998.

[37] T. S. Ibrahim, R. Lee, B. A. Baertlein, and P. M. L. Robitaille, "B-1 field homogeneity and SAR calculations for the birdcage coil," *Phys Med Biol*, vol. 46, pp. 609-619, Feb 2001.

[38] T. S. Ibrahim and L. Tang, "Insight into RF power requirements and B1 field homogeneity for human MRI via rigorous FDTD approach," *J Magn Reson Imaging*, vol. 25, pp. 1235-47, Jun 2007.

[39] J. Jin and J. Chen, "On the SAR and field inhomogeneity of birdcage coils loaded with the human head," *Magn Reson Med*, vol. 38, pp. 953-63, Dec 1997.

[40] R. Lattanzi, D. K. Sodickson, A. K. Grant, and Y. Zhu, "Electrodynamic constraints on homogeneity and radiofrequency power deposition in multiple coil excitations," *Magn Reson Med*, vol. 61, pp. 315-34, Feb 2009.

[41] W. Liu, C. M. Collins, P. J. Delp, and M. B. Smith, "Effects of end-ring/shield configuration on homogeneity and signal-to-noise ratio in a birdcage-type coil loaded with a human head," *Magn Reson Med,* vol. 51, pp. 217-21, Jan 2004.

[42] C. Wang and G. X. Shen, "B1 field, SAR, and SNR comparisons for birdcage, TEM, and microstrip coils at 7T," *J Magn Reson Imaging,* vol. 24, pp. 439-43, Aug 2006.

[43] E. M. Haacke, *Magnetic resonance imaging : physical principles and sequence design*. New York: Wiley, 1999.

[44] D. I. Hoult and R. E. Richards, "The signal-to-noise ratio of the nuclear magnetic resonance experiment. 1976," *J Magn Reson,* vol. 213, pp. 329-43, Dec 2011.

[45] G. Jost, I. Harting, and S. Heiland, "Quantitative single-voxel spectroscopy: the reciprocity principle for receive-only head coils," *J Magn Reson Imaging,* vol. 21, pp. 66-71, Jan 2005.

[46] V. Barra and J. Y. Boire, "Segmentation of fat and muscle from MR images of the thigh by a possibilistic clustering algorithm," *Comput Methods Programs Biomed,* vol. 68, pp. 185-93, Jun 2002.

[47] K. E. Schreiner, "The helix as propeller of microorganisms," *J Biomech,* vol. 4, pp. 73-83, Jan 1971.

[48] L. Zhang, J. J. Abbott, L. Dong, K. E. Peyer, B. E. Kratochvil, H. Zhang, C. Bergeles, and B. J. Nelson, "Characterizing the swimming properties of artificial bacterial flagella," *Nano Lett,* vol. 9, pp. 3663-7, Oct 2009.

[49] R. Dreyfus, J. Baudry, M. L. Roper, M. Fermigier, H. A. Stone, and J. Bibette, "Microscopic artificial swimmers," *Nature,* vol. 437, pp. 862-5, Oct 6 2005.

[50] A. Ghosh and P. Fischer, "Controlled propulsion of artificial magnetic nanostructured propellers," *Nano Lett,* vol. 9, pp. 2243-5, Jun 2009.

[51] L. Zhang, K. E. Peyer, and B. J. Nelson, "Artificial bacterial flagella for micromanipulation," *Lab Chip,* vol. 10, pp. 2203-15, Sep 7 2010.

[52] J. Burdick, R. Laocharoensuk, P. M. Wheat, J. D. Posner, and J. Wang, "Synthetic nanomotors in microchannel networks: directional microchip motion and controlled manipulation of cargo," *Journal of the American Chemical Society,* vol. 130, pp. 8164-5, Jul 2 2008.

[53] J. Happel and H. Brenner, *Low Reynolds number hydrodynamics With special applications to particulate media*, 2d rev. ed. Leyden,: Noordhoff International Publishing, 1973.